ANNUAL REVIEWS

Annual Review of Materials Research

Materials for Gamma-Ray Spectrometers: Inorganic Scintillators

Douglas S. McGregor

Mechanical and Nuclear Engineering Department and SMART Laboratory, Kansas State University, Manhattan, Kansas 66506, USA; email: mcgregor@ksu.edu

Annu. Rev. Mater. Res. 2018.48:245-277. Downloaded from www.annualreviews.org
Access provided by Kansas State University on 09/24/18. For personal use only.

ANNUAL REVIEWS **Further**

Click here to view this article's online features:

- Download figures as PPT slides
- Navigate linked references
- Download citations
- Explore related articles
- Search keywords

Annu. Rev. Mater. Res. 2018. 48:245–77

First published as a Review in Advance on April 4, 2018

The *Annual Review of Materials Research* is online at matsci.annualreviews.org

https://doi.org/10.1146/annurev-matsci-070616-124247

Copyright © 2018 by Annual Reviews.
All rights reserved

Keywords

gamma ray, scintillators, spectrometers

Abstract

Scintillation detectors constitute an important branch of radiation detection instrumentation. The discovery of the inorganic scintillating compound thallium-activated sodium iodide (NaI:Tl) in 1948 was key to the production of the first practical gamma-ray spectrometer. Since that time, numerous inorganic scintillators have been discovered and studied. Many of the more successful inorganic scintillators are described, including discussion of their properties and performance, in this article.

Annu. Rev. Mater. Res. 2018.48:245-277. Downloaded from www.annualreviews.org
Access provided by Kansas State University on 09/24/18. For personal use only.

1. INTRODUCTION

Gamma-ray detectors have been under progressive development from the initial identification of X-rays by Wilhelm Röntgen in 1895. The detector that was used to discover X-rays was a plate coated with a scintillation material, barium platino-cyanide [$BaPt(CN)_4$]. The introduction of the first commercial photomultiplier tube (PMT) in 1941, the RCA 931A, provided a means to effectively measure small emissions of light from scintillators. The first demonstrations of scintillator/PMT systems were conducted with organic scintillators attached to PMTs (1). Because organic scintillators are composed of low-Z materials, they are relatively inefficient as gamma-ray detectors and are not considered in this review. The discovery of thallium-activated sodium iodide (NaI:Tl) by Robert Hofstadter in 1948 led to the first efficient PMT/scintillator gamma-ray spectrometer. Described in this short review are many inorganic scintillator materials that either are commercially available or have reasonable potential as gamma-ray spectrometers.

2. THE SCINTILLATION PROCESS

The scintillation process is described elsewhere as consisting of five distinctive stages (2), namely

1. radiation absorption and subsequent excitation of electron-hole pairs,
2. relaxation of primary electron-hole pairs,
3. thermalization of the charge carriers,
4. energy transfer to luminescent centers, and
5. photon emission from the luminescent centers.

Usually, processes 1–3 are grouped as electron-hole production, and processes 4 and 5 are grouped as photon emission. An ionizing particle excites multiple electron-hole pairs by various ionizing processes, including photoionization, elastic and inelastic scattering, Coulombic scattering, fission, and neutron transmutation. The initial ionizing event also produces a cascade of delta rays, which excite more electron-hole pairs. The process by which the holes relax is either from radiative transitions, in which an outer shell electron falls into the empty state by releasing a photon (a characteristic X-ray), or by a nonradiative transition (i.e., Auger electron emission). These subsequent emissions can be reabsorbed by outer shell electrons of nearby atoms, thereby producing more electron-hole pairs.

Meanwhile, the liberated energetic electrons travel through the crystal lattice and lose energy through Coulombic interactions and, thus, liberate more electron-hole pairs. The process continues until the resultant electrons and holes no longer have sufficient energy to produce more ionization. Overall, electrons and holes drop to their respective band edges, electrons at the conduction band edge and holes at the valence band edge, within approximately 10^{-15}–10^{-13} s. Excited electrons still bound to their respective holes through Coulombic forces are also formed at this stage. This condition causes the electron-hole pair to have slightly lower energy than a free electron-hole pair. Thus, the pair exists at an energy below the band gap energy E_g and diffuses together as an electrical neutral quasi-particle termed an exciton.

Inorganic scintillators depend primarily on the crystalline energy band structure of the material for the scintillation mechanism. **Figure 1** shows an energy band diagram for a typical inorganic scintillator. If a radiation particle interacts in the scintillation material, it can excite numerous electrons from the valence and lower-bound bands up into the conduction bands (see **Figure 1*a***). These electrons rapidly lose energy and fall to the conduction band edge E_C. As they deexcite and drop back into the valence band, they can lose energy through light emissions. If the radiated energy is equivalent to E_g, the radiated photons can be reabsorbed, and the scintillator is essentially opaque to its own emissions.

Annu. Rev. Mater. Res. 2018.48:245-277. Downloaded from www.annualreviews.org
Access provided by Kansas State University on 09/24/18. For personal use only.

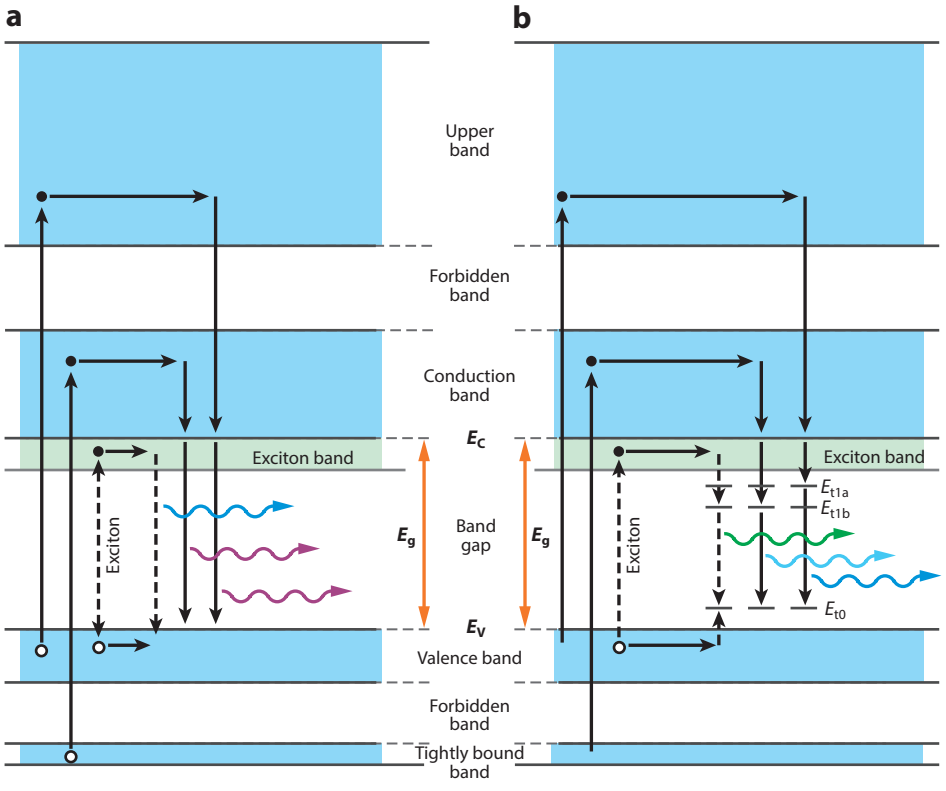

Figure 1

Two basic methods by which an inorganic scintillator produces light: (*a*) the intrinsic case and (*b*) the extrinsic case. The colored arrows represent photon emissions of different wavelengths from the intrinsic (*left*) and extrinsic (*right*) cases. The activated extrinsic case generally has longer wavelength (lower energy) emissions than the intrinsic case. Abbreviations: E_C, conduction band edge; E_g, band gap energy; E_{t0}, activator ground state; E_{t1a}, activator excited state; E_{t1b}, activator excited state; E_V, valence band edge.

An impurity added to the crystal can introduce allowed states in the band gap (depicted in **Figure 1*b***), termed an activated scintillator. The excitation process remains similar to that of the intrinsic case. However, a significant fraction of electrons can fall into the activator excited state. Transitions to the activator ground state release sub-band-gap photon energies and avoid reabsorption. There are exceptions in which intrinsic scintillators work well without activators; examples are bismuth germanate ($Bi_4Ge_3O_{12}$ or BGO) and barium fluoride (BaF_2).

The light emission spectrum is dependent on the activator choice and is usually spread over a continuum of energies. The coordinate configuration diagram of **Figure 2** can be used to explain the emission spectrum. An electron can be excited to point *B* by excitation from point *A*, can be captured from the conduction band, or can experience exciton capture. The transition causes thermal motion and vibrational states to appear, represented as horizontal lines in **Figure 2**. Both the spatial occupancy and the electron wave function change with this transition to the excited state, and the spatial position of lowest energy changes from *A* to Q_{e0}. The electron rapidly loses energy and moves to location *C* and can drop to location *E*, releasing a photon. The electron thermally loses energy and returns to location *A*.

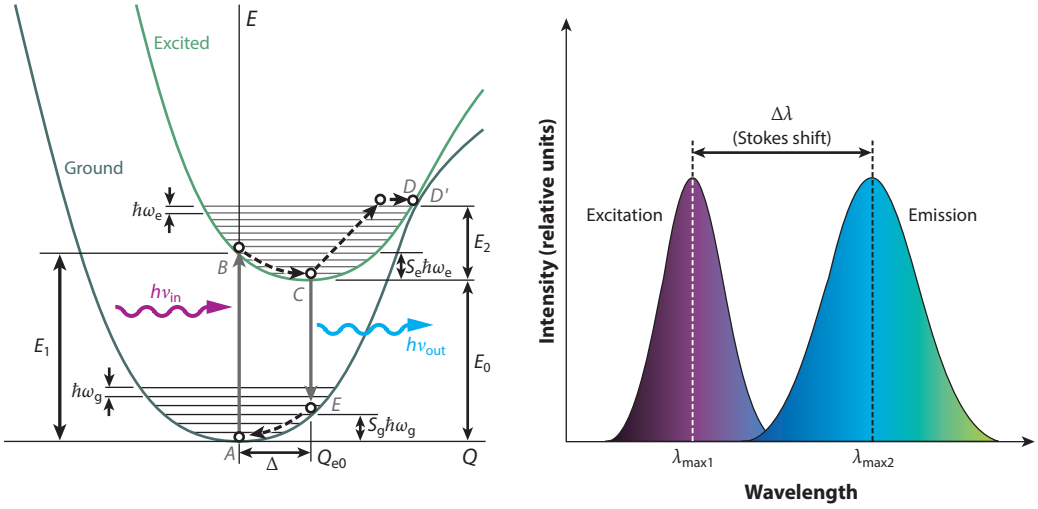

Figure 2

Configuration coordinate diagram depicting Stokes shift luminescence and a form of nonradiative deexcitation. The ordinate is energy E, and the abscissa is the average distance Q between the luminescent center and surrounding ions. Definitions: e, excited state; E_0, energy difference between lowest excited state and lowest ground state; E_1, excitation energy from ground state to excited state; E_2, energy difference between upper and lower excited vibrational states; g, ground state; $h\nu_{in}$, absorbed photon energy; $h\nu_{out}$, emitted photon energy; $\hbar\omega$, vibrational state energy; S, number of vibrational states; $S\hbar\omega$, total energy of vibrational states; Δ, interatomic displacement of excited electron; λ_{max1}, most probable absorption wavelength; λ_{max2}, most probable emission wavelength.

The excitation energy ($A \rightarrow B$) is larger than the emission energy ($C \rightarrow E$). This change causes the resultant absorption spectrum of a luminescent center to be different from the emission spectrum because the absorption spectrum is centered about shorter wavelengths than is the centroid of the emission wavelengths. This shift in wavelength is known as the Stokes shift:

$$\Delta\lambda = \lambda_{\max_E} - \lambda_{\max_A}. \quad 1.$$

If the Stokes shift is adequately large, photon emissions have too little energy to be reabsorbed by the scintillation crystal or other luminescent centers.

At a given temperature T, the emission probability can be modeled as a Gaussian distribution (3)

$$W(\hbar\omega) = \frac{1}{\sqrt{2\pi}\sigma} \exp\left[\frac{-[(1+S)\hbar\omega - E_0)]^2}{2\sigma^2}\right], \quad 2.$$

where S is the number of vibration states for the transition $C \rightarrow E \rightarrow A$, $\hbar\omega$ is the phonon energy, E_0 is the energy difference between the excited state minimum and the ground state minimum, and $\hbar$ is the reduced Planck constant. If the vibrational mode angular frequencies are identical for the excited and ground states, then the variance as a function of temperature is

$$[\sigma(T)]^2 \approx 2S_g kT\hbar\omega, \quad 3.$$

which defines the spectral broadening of the emission spectrum, $w = 2.355\sigma_e$, where k is Boltzmann's constant. From Equation 3, it is observed that the variance of the emission spectrum increases with S_g, ω, and the absolute temperature T.

The potential energy curves depicted in **Figure 2** often intersect or come close along the Q direction, represented as points D and D'. With thermal agitation, the electron can move directly

Annu. Rev. Mater. Res. 2018.48:245-277. Downloaded from www.annualreviews.org
Access provided by Kansas State University on 09/24/18. For personal use only.

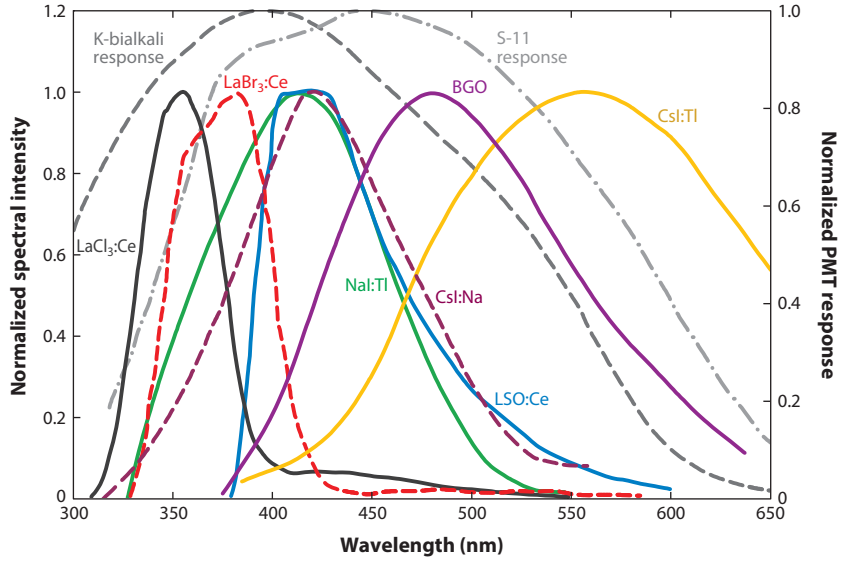

Figure 3

The emission spectra from several popular inorganic scintillators. Also shown is an overlaying sensitivity comparison to the normalized responses of two common photomultiplier tubes (PMTs) (K-bialkali and S-11). Abbreviations: BGO, $Bi_4Ge_3O_{12}$; LSO, Lu_2SiO_5. Scintillation spectral response data from References 4–6. PMT response data from Reference 7.

to the ground state without releasing a photon. The excess energy is lost to phonon emission and does not contribute to the fluorescent light yield (thermal quenching).

Delayed emissions can occur if electrons fall into metastable states with forbidden ground transitions. Thermal energy from the ambient environment may reexcite the electrons to allowed transitions, but the return to allowed transitions is usually delayed beyond several decay times for fluorescent photons. These delayed photon emissions are termed phosphorescence or afterglow. These afterglow light emissions can be detected, but the time delay decouples their correlation with the original radiation absorption event.

3. THE SCINTILLATION DETECTOR

For the best results, the scintillation spectra and light sensor response should be matched. The most common device used to detect the relatively low light emissions from a scintillator is a PMT. **Figure 3** shows numerous emission spectra from common scintillators, along with two comparison responses of two common PMTs.

A typical scintillation spectrometer consists of a hermetically sealed scintillator in a light-reflecting canister. An optical compound between the scintillator and light collector reduces reflective losses. The light collector is used to provide a linear voltage output as an indication of the radiation energy spectrum deposited in the scintillator. Commercial detectors are typically sold as a single complete unit (depicted in **Figure 4**), although individual parts can be acquired separately. The device is connected to a readout system, typically a multichannel analyzer that is used to collect and organize voltage pulses into a histogram as a function of pulse magnitude.

Annu. Rev. Mater. Res. 2018.48:245-277. Downloaded from www.annualreviews.org
Access provided by Kansas State University on 09/24/18. For personal use only.

Annu. Rev. Mater. Res. 2018.48:245-277. Downloaded from www.annualreviews.org
Access provided by Kansas State University on 09/24/18. For personal use only.

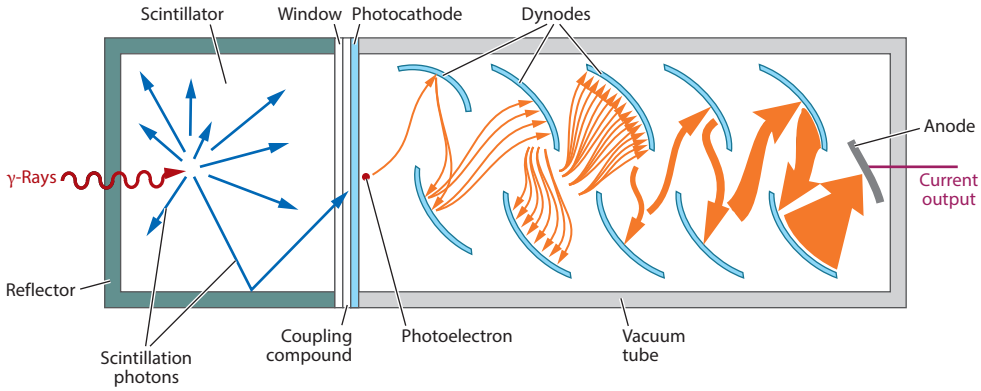

Figure 4

The basic construction of a scintillation detector. A scintillation photon that strikes the photocathode creates a photoelectron. The photoelectron is accelerated and guided to the first dynode by an electric field, where it strikes the dynode and ejects more electrons. These electrons are accelerated to the next dynode and excite more electrons. The process continues through the dynode chain until the cascade of electrons is collected at the anode, whose output current is used to produce a voltage pulse.

3.1. The Photomultiplier Tube

The PMT includes (*a*) a transparent envelope, usually glass; (*b*) a photocathode; (*c*) a series of dynodes; and (*d*) an anode. The basic PMT, depicted in **Figure 4**, has a photocathode that is located to absorb light emissions from the scintillator. Photons that strike the photocathode excite electrons that can diffuse to the vacuum surface of the PMT; some of the electrons that diffuse to the vacuum interface retain sufficient energy to escape into the vacuum tube. Photocathodes are generally fabricated from alkaline metals, which are most sensitive to light with wavelengths in the 350–450-nm range. Under some circumstances, PMTs can be used by scintillators emitting light outside this range, although their effectiveness may be severely compromised.

A steering voltage guides the free electrons to an adjacent electrode termed a dynode. The kinetic energy liberates more electrons from the dynode, and these newly liberated electrons are then guided by the electric field to the next dynode and so on. The total charge released in the PMT is

$$Q = q\bar{N}\bar{p}\bar{G} = qN_0\prod_{i=1}^{M}\bar{g}_i, \qquad 4.$$

where $\bar{N}$ is the average scintillation light yield at a particular energy, $\bar{p}$ is the conversion or transfer efficiency of these photons into photoelectrons at the photocathode, $\bar{G}$ is the overall average total PMT gain, q is the charge of an electron, N_0 is the initial number of photoelectrons released at the photocathode, $\bar{g}_i$ is the average number of electrons released per dynode (the gain), and M is the total number of dynodes. It is this electrical signal, converted to a voltage pulse, that is measured. A PMT with 10 dynodes, each having $\bar{g}_i = 4$, can produce 10^9 electrons from the initial release of only 1,000 electrons (N_0) at the photocathode. Hence, the PMT transforms a small amount of light into a large electrical signal. PMTs are stable and electronically quiet (low noise). Modern varieties have exceptional photocathode and dynode efficiencies, often referred to as quantum efficiencies, with gains that can exceed 30 per surface.

3.2. The Silicon Photomultiplier

The silicon photomultiplier (SiPM) has become available and in some cases is replacing the traditional PMT. For any *pn* junction operated with a reverse bias voltage, there is a voltage at which the junction freely conducts current, a condition termed avalanche breakdown. After the avalanche is triggered, the self-sustained current continues to flow unless quenched. Quenching can be accomplished with a load resistor in series with the *pn* junction diode. As current increases, the voltage increases across the resistor, causing the voltage to decrease across the diode. When the voltage on the diode drops below a critical value, the avalanching stops. Avalanche photodiodes (APDs) designed and operated in this mode are often said to operate in so-called Geiger mode (8). SiPMs use this breakdown condition with thousands of tiny APDs arranged into a compact array on the order of 6 mm × 6 mm total size (or less).

A scintillator may be fastened to the SiPM face, and light from radiation interactions within the scintillator triggers the APDs. Each APD provides information that is ultimately limited to recognizing the excitation of an electron-hole pair within the sensitive region. Each APD pixel produces an avalanche of relatively the same magnitude per event. Hence, the total photon count can be determined by dividing the total measured charge by the avalanche gain. When all currents (or charges) from each APD are added together, a SiPM can provide $>10^9$ free electrons per event.

A particular advantage of SiPMs is the high quantum efficiency of Si for photons with wavelengths between 350 nm and 950 nm. The photon detection efficiency of a SiPM can be much higher than that of a common PMT. However, many commercial SiPM units are designed with peak sensitivity near 420 nm, similar to conventional bialkali PMTs. SiPMs are compact and rugged—perhaps some of their most useful features. They need only modest power, usually requiring no more than a few tens of volts for operation. SiPMs are also insensitive to magnetic fields, thereby making them an attractive choice for applications in areas where high magnetic fields may arise.

3.3. Energy Resolution

The energy resolution of a radiation spectrometer is defined as the full width of the spectroscopic energy peak (usually ΔE) at half the maximum intensity (FWHM). The energy resolution from scintillators is traditionally reported in terms of percent of the most probable energy (the mode) in the pulse height spectrum,

$$R_{\%} = 100\left(\frac{\mathrm{FWHM}}{E_{\max}}\right). \quad 5.$$

The minimum value of the FWHM can be modeled, to a first approximation, with Poisson statistics; i.e.,

$$\mathrm{FWHM} = 2\sqrt{2\ln(2)\mathrm{var}(E)}, \quad 6.$$

where var(E) is the variance of the full energy peak in the pulse height spectrum. **Figure 5** depicts a FWHM in an example gamma-ray pulse height spectrum taken with a NaI:Tl detector. If the scintillator is coupled to a PMT light detector, the light collected is converted to an electron signal. Hence, the variance in the number of electrons collected by the PMT is a measure of the variance of the pulse height spectrum, or $\sqrt{\mathrm{var}(E)}/E_{\max} \approx \sqrt{\mathrm{var}(Q)}/Q_{\max}$. The fractional variance in electrons collected by the PMT can be expressed as

$$v(Q) = \frac{\mathrm{var}(Q)}{\bar{Q}^2} = \left[\frac{\mathrm{var}(N)}{\bar{N}^2} - \frac{1}{\bar{N}}\right]\left[1 + \frac{\mathrm{var}(p)}{\bar{p}^2}\right] + \frac{\mathrm{var}(p)}{\bar{p}^2} + \frac{\bar{G}^2 + \mathrm{var}(G)}{\bar{G}^2\bar{N}\bar{p}}, \quad 7.$$

Annu. Rev. Mater. Res. 2018.48:245-277. Downloaded from www.annualreviews.org
Access provided by Kansas State University on 09/24/18. For personal use only.

Annu. Rev. Mater. Res. 2018.48:245-277. Downloaded from www.annualreviews.org
Access provided by Kansas State University on 09/24/18. For personal use only.

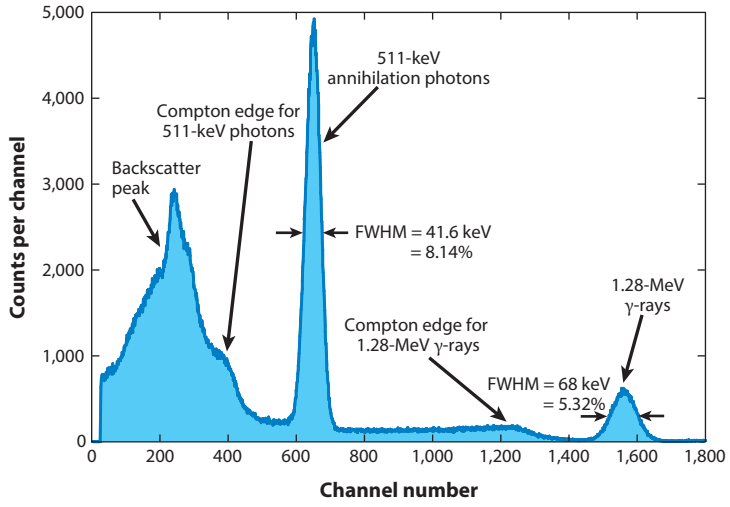

Figure 5

Pulse height spectrum of ^{22}Na taken with a 2 × 2 inch NaI:Tl detector. Abbreviation: FWHM, full width at half-maximum.

where var(N) is the variance in the number of scintillation photons, var(p) is the transfer variance, and var(G) is the variance in the PMT gain (see References 9 and 10). For an ideal scintillator based on Poisson statistics, var(N) = $\bar{N}$ and var(p) = 0. Consequently, Equation 7 reduces to

$$v(Q) \approx \frac{1 + \mathrm{var}(G)/\bar{G}^2}{\bar{N}\bar{p}}, \qquad 8.$$

where the product $\bar{N}\bar{p}$ represents the number of photoelectrons produced. Values for var(G)/$\bar{G}^2$ are usually between 0.1 and 0.2 (11). The ideal best energy resolution of a scintillation detector becomes

$$\mathrm{FWHM} \approx 2\sqrt{2\ln(2)}\sqrt{\frac{1+0.1}{\bar{N}\bar{p}}} = 2.355\sqrt{\frac{1+0.1}{\bar{N}\bar{p}}}. \qquad 9.$$

This ideal energy resolution is plotted as a solid line in **Figure 6** and is compared to measured values of many common inorganic scintillators. Almost all scintillators shown in **Figure 6** fall short of the predicted ideal energy resolution. Factors that broaden energy resolution include nonproportional light yield, poor light reflection in the encapsulate, crystal transparency and imperfections, and index-of-refraction mismatch.

3.4. Light Yield

The absolute light yield is the total number of fluorescent photons released per unit absorbed energy, typically reported as photons per megaelectron volt. The absolute light yield is usually reported for a specific energy, although a multitude of gamma-ray energies may be used for calibration (see Reference 14). For statistical reasons, a high absolute light yield is desirable for good gamma-ray energy resolution. Absolute light yields of several common inorganic scintillators are listed in **Table 1**. The relative light yield is the number of photons emitted per unit energy at different energies, usually normalized at a specific energy. Recent works normalize the relative

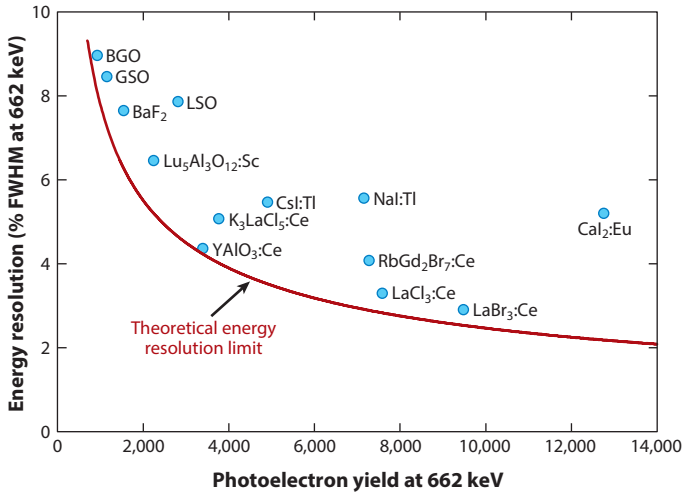

Figure 6

Measured energy resolution for several inorganic scintillating materials. Also shown is the theoretical limiting energy resolution. Abbreviations: BGO, $Bi_4Ge_3O_{12}$; FWHM, full width at half-maximum; GSO, Gd_2SiO_5; LSO, Lu_2SiO_5. Adapted from Reference 11 with permission.

light yield at 450 keV (15–17). The relative light yield is a measure of the fluorescent linearity to absorbed energy. Ideally, the relative light yield should be constant across all energies; however, several physical factors cause deviation (18).

Although the cause of nonlinear light yield is not fully understood, progress has been made in recent years with predictive modeling (17, 19, 20). An important factor affecting nonproportionality is the ionization density produced by an interacting charged particle (electron). From the Bethe-Bloche expression for electron energy loss in matter, the ionization density increases as the electron velocity (or energy) decreases. For most scintillators, there is a notable decrease in relative light yield in the low-energy region (as shown in **Figures 7** and **8**), which indicates that light yield for these scintillators decreases as ionization density increases. However, for several alkali-metal/halogen scintillators, there is a notable decrease in light yield also in the high-energy region (see **Figure 7**), an indication that the relative light yield is decreasing for low ionization densities. This ionization density is dependent upon the initial excitation energy of the ejected electron produced by Compton scattering, pair production, or the photoelectric effect. Furthermore, the deexcitation processes, radiative or nonradiative, are also dependent on the incident particle energy. Numerous models are proposed to predict or explain the relative light yield of inorganic scintillators (20).

The minimalist model seeks to explain nonproportionality as losses from collisions between excitons, where one exciton pair becomes an electron-hole pair that deexcites by nonradiative transitions while the other exciton is preserved. The probability of this event increases with the square of the charge carrier density and becomes dominant at low energies. At higher energies, the electron and hole densities are lower and spatially separated. Electrons and holes within the Onsager radius R_O can form mobile excitons.[1] On the basis of the nonlinear behavior described

[1]The Onsager radius is the physical distance between an electron and a hole, where the electrostatic energy equals the thermal energy, i.e., $q^2/(\epsilon R_O) = kT$, where ϵ is the dielectric constant and q is the unit electronic charge. At $R < R_O$, the electron (or hole) cannot escape from the Coulombic force field (19).

Annu. Rev. Mater. Res. 2018.48:245-277. Downloaded from www.annualreviews.org
Access provided by Kansas State University on 09/24/18. For personal use only.

Table 1 Common inorganic scintillator materials and properties

Scintillator	Density (g/cm^3)	Z	Refractive index (at λ_{max})	λ_{max} (nm)	Decay time (ns)	Light yield (photons/MeV)	Bialkali PMT response WRT NaI:Tl
CsI (fast)	4.51	55, 53	1.95	315	16	2,000	0.04–0.06
CsI (slow)	4.51	55, 53	1.95	450	1,000	~200	ND
CsI:Na	4.51	55, 53	1.84	420	460, 630, 1,800	41,000–49,000	0.85
CsI:Tl	4.51	55, 53	1.79	550	600, 3,500	54,000–61,000	0.45
LiI:Eu	4.08	3, 53	1.96	475	1,400	15,000	0.35
NaI:Tl	3.67	11, 53	1.82	415	230	43,000	1.00
BaF_2 (fast)	4.88	56, 9	1.54	220	0.6–0.8	1,800	0.03
BaF_2 (slow)	4.88	56, 9	1.5	310	630	10,000	0.16
CaF_2:Eu	3.18	20, 9	1.44	435	900	24,000	0.50
CaI_2	3.96	20, 53	1.8	410	550	86,000	ND
CaI_2:Eu	3.96	20, 53	1.8	470	790	86,000	ND
$CaWO_4$	6.1	20, 74, 8	1.94	425	8,000	~20,000	ND
SrI_2:Eu	4.55	38, 53	1.85	435	1,200	115,000	ND
$CdWO_4$	7.90	48, 74, 8	2.30	470	14,000	~1,350	0.3–0.5
$YAlO_3$:Ce	5.35	39, 13, 8	1.95	370	27	18,000	0.45
$Y_3Al_5O_{12}$:Ce	4.55	39, 13, 8	1.82	550	88, 302	17,000	0.50
Y_2SiO_5:Ce	4.45	39, 14, 8	1.8	420	56	24,000	ND
ZnS:Ag	4.09	30, 16	2.36	450	110	50,000	1.3
$Bi_4Ge_3O_{12}$	7.13	83, 32, 8	2.15	480	300	8,200	0.13
$CeBr_3$	5.2	58, 35	2.09	371	17	68,000	ND
Gd_2SiO_5	6.71	64, 14, 8	1.85	440	56, 400	9,000	0.20
$LaCl_3$:Ce	3.86	57, 17	2.05	350	28	49,000	0.70–0.90
$LaBr_3$:Ce	5.29	57, 35	2.05	380	16	63,000	1.65
$LuAlO_3$:Ce	8.34	71, 13, 8	1.94	365	16.5, 74	11,400	ND
$Lu_3Al_5O_{12}$:Pr	6.71	71, 13, 8	1.84	310	20–22	~18,000	ND
Lu_2SiO_5:Ce	7.4	71, 14, 8	1.82	420	47	25,000	0.75
$Lu_{1.8}Y_{0.2}SiO_5$:Ce	7.1	71, 39, 14, 8	1.82	420	41	32,000	0.75
Cs_2LiYCl_6	3.31	55, 3, 39, 17	1.81	305	6, 600	6,535, 22,420	ND
Cs_2LiYCl_6:Ce	3.31	55, 3, 39, 17	1.81	372, 400	600, 6,000	9,565, 18,400	ND
$Cs_2LiLaBr_6$:Ce	4.2	55, 3, 57, 35	1.85	420	180, 1,100	43,000	1.15
Li glass:Ce	2.5	NA	1.55	395	(n) 18, 57 (α) 16, 49 (β) 20, 58	~4,650	~0.12
Tb glass	3.0–3.52	NA	1.5–1.62	550	3–5 ms	13,000–50,000	ND

Abbreviations: NA, not applicable; ND, no data; PMT, photomultiplier tube; WRT, with respect to. Data from References 6, 13, 21–35, and 138.

by Birks (9), the light yield thus becomes

$$L = \frac{1 - \eta_{eh} \exp\left[-\frac{dE/dx}{(dE/dx)_{R_O}}\right]}{1 + kB\frac{dE}{dx}}, \qquad 10.$$

where η_{eh} is the fraction of electrons and holes that do not form excitons; (dE/dx) is the ionization density; $(dE/dx)_{R_O}$ is the linear energy loss, where the average electron-hole spacing is R_O; and

Annu. Rev. Mater. Res. 2018.48:245-277. Downloaded from www.annualreviews.org
Access provided by Kansas State University on 09/24/18. For personal use only.

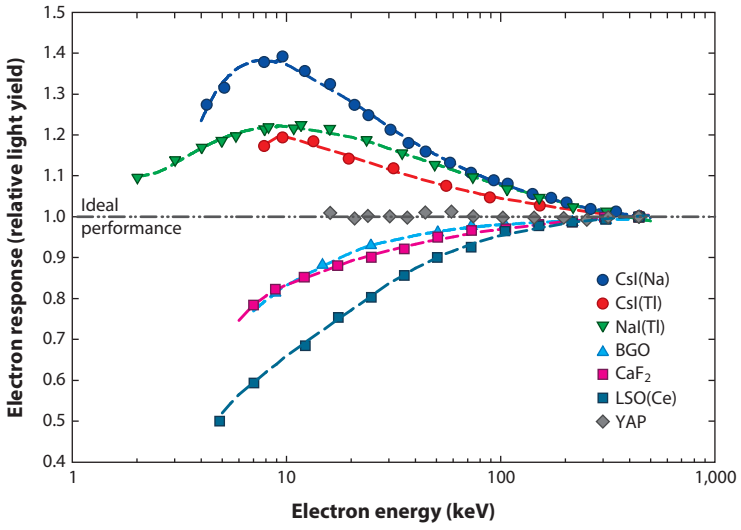

Figure 7

Relative light yield for several inorganic scintillating materials, normalized at 440 keV. Abbreviations: BGO, $Bi_4Ge_3O_{12}$; LSO, Lu_2SiO_5:Ce; YAP, $YAlO_3$:Ce. Data are from Reference 15 and are reproduced with permission.

kB is the quenching parameter described by Birks (9). Payne et al. (17) successfully apply Equation 10 to model numerous scintillator materials. Not based on first principles, the minimalist model is nonpredictive and more akin to an empirical data curve fitting.

The kinetic model includes known phenomena, including trap-assisted radiative emission charge carrier reduction from recombination, that affect scintillation yield but that are disregarded

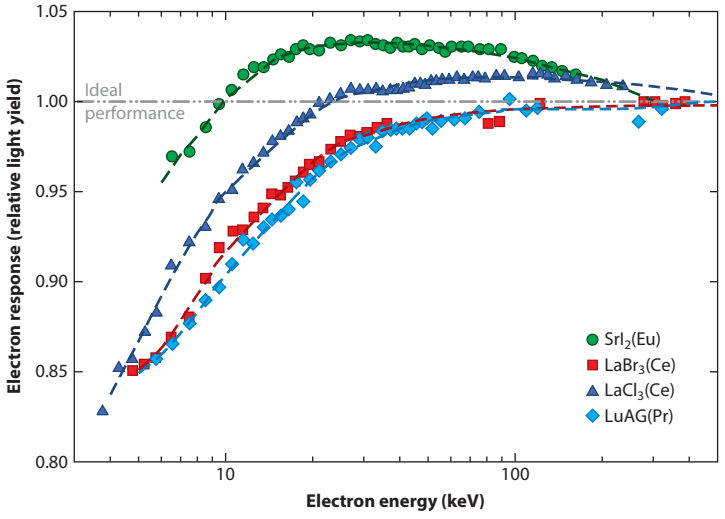

Figure 8

Relative light yield for several inorganic scintillating materials, normalized at 450 keV. Abbreviation: LuAG, $Lu_3Al_5O_{12}$:Pr. Data are from References 16 and 17 and are reproduced with permission.

Annu. Rev. Mater. Res. 2018.48:245-277. Downloaded from www.annualreviews.org
Access provided by Kansas State University on 09/24/18. For personal use only.

Annu. Rev. Mater. Res. 2018.48:245-277. Downloaded from www.annualreviews.org
Access provided by Kansas State University on 09/24/18. For personal use only.

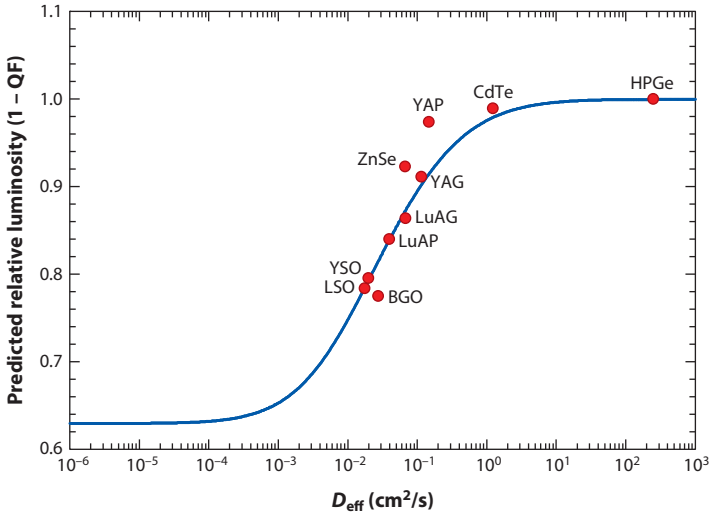

Figure 9

Measured relative light yield at low electron energy for several common scintillators compared to the predicted results from a diffusion model. The responses are shown as functions of diffusion coefficients. The term (1 − QF) is the fraction of carriers that survive at least 10 ps after the charge cloud is formed. CdTe and HPGe are semiconductors, and the measured metric is the charge carrier collection efficiency. Abbreviations: BGO, $Bi_4Ge_3O_{12}$; D_{eff}, diffusion coefficient; HPGe, high-purity Ge; LSO, Lu_2SiO_5:Ce; LuAG, $Lu_3Al_5O_{12}$:Ce, LuAP, $LuAlO_3$:Ce; QF, quenched fraction; YAG, $Y_3Al_5O_{12}$:Ce; YAP, $YAlO_3$:Ce; YSO, Y_2SiO_5:Ce. Adapted from Reference 36 with permission.

in the minimalist model. Through either rigorous mathematical rate equations or Monte-Carlo techniques, these kinetic models attempt to track changes in the electron-hole-exciton cloud as a function of time. Although such models are complicated, the stated advantage is insight into the scintillation mechanism (20).

The diffusion model includes the effect of electron and hole mobility and ambipolar diffusion of excitons, and it can be used to modify the kinetic model. The model has at least three major implications (20). First, if one charge carrier type diffuses much faster than the other, then the charge carriers become physically separated, and recombination significantly decreases. Second, for materials with similar electron and hole diffusion coefficients, both carriers diffuse with similar spatial distributions, thereby producing a high light yield by efficient recombination. Third, charge carriers and excitons with high mobilities rapidly separate, diminishing the carrier density and reducing quenching losses. Consequently, scintillation materials with high charge carrier mobilities are expected to have proportional light output, while the opposite is the case for materials with low charge carrier mobilities. The diffusion model has been successfully used to predict luminosity from several common scintillators (36). **Figure 9** shows a comparison of empirical measurements of proportionality with the diffusion model predictions.

A scintillator is said to have a linear response if the light yield scales as

$$\langle N \rangle = k_1 E + b, \qquad 11.$$

where $\langle N \rangle$ is the mean number of information carriers, E is the absorbed radiation energy, k_1 is a proportionality constant, and b is a constant. For scintillators, $\langle N \rangle$ is the average number of photons produced per event at energy E. In such a case, the scaling of a scintillator is predictable, but the average energy needed to produce a photon is a function of energy and is not constant.

If the constant b is zero, the scintillator is said to have a proportional response, in which case $w = E/\langle N\rangle$ is constant. Regardless of the value of b, the differential change in information carriers per differential change in energy is constant, or $\mathrm{d}\langle N\rangle/\mathrm{d}E$ is constant for both linear and proportional responses.

Nonlinear (or nonproportional) light yield response as a function of energy complicates energy calibration (18). Ideally, the relative light yield should be constant, or at least proportional, for all energies. Consequently, spectral features do not appear in channels predicted with a linear formula. Predictive modeling can be used to develop a reasonably accurate scaled response. Large deviations in relative light yield as a function of energy adversely affect the resolution by increasing statistical spread in the photon yield (37). Two factors identified by Valentine et al. (37) that contribute to energy resolution broadening are (*a*) multiple interaction events resulting in one or more energetic primary electrons prior to photoelectric absorption and (*b*) the resulting electron cascade sequence that follows photoelectric absorption that produces Auger electrons and X-ray emissions.

Annu. Rev. Mater. Res. 2018.48:245-277. Downloaded from www.annualreviews.org
Access provided by Kansas State University on 09/24/18. For personal use only.

3.5. Decay Time and Pulse Formation

Suppose that a radiation particle interacts in a material and excites N^* electron-hole pairs. Of these N^* electrons, an average fraction of electrons fall into luminescent centers, represented by $N = fN^*$, where the probability λ_r of falling into a luminescent center is related to the rise time by $\lambda_r = 1/\tau_r$. The luminescent center population $N_c(t)$ immediately after a radiation interaction is

$$N_c(t) = N\frac{\tau_d}{\tau_r - \tau_d}\left(e^{-t/\tau_r} - e^{-t/\tau_d}\right), \qquad 12.$$

where τ_d is the decay time of the luminescent center. The light emission rate, in photons per unit time, is expressed as a function of the decay time,

$$L(t) = \frac{N_c(t)}{\tau_d} = \frac{N}{\tau_r - \tau_d}\left(e^{-t/\tau_r} - e^{-t/\tau_d}\right). \qquad 13.$$

If the population rise time is extremely short (less than or equal to a few nanoseconds), which it usually is, then Equation 13 reduces to

$$L(t) \simeq \frac{N}{\tau_d}\left(e^{-t/\tau_d}\right). \qquad 14.$$

The solution of Equation 13 is derived with the assumption that a single decay time can adequately represent the light emission rate of a scintillation material. The decay times listed in **Table 1** are average values obtained from experiment. Many luminescent states may play a part in the emission sequence. These decay times for separate energy levels are often similar enough that an average decay time adequately defines the light emission behavior. However, many scintillators have multiple decay times that are notably different. Some scintillators also have different emission wavelengths. In **Table 1**, CsI:Na, CsI:Tl, and BaF_2 are examples of scintillators with multiple decay times. In fact, there is a significant difference in the decay times and the maximum wavelengths λ_{max} for BaF_2 emissions.

3.6. Thermal Properties

From **Figure 2** and the explanation offered in Section 2, scintillation light yield at high temperatures (>100°C) generally results in a reduction in light yield. One cause of the reduction is the increased numbers of excited electrons lost from direct transfer from the excited state to the ground state (38). Another source of a decrease in the maximum light yield is the increase

Annu. Rev. Mater. Res. 2018.48:245-277. Downloaded from www.annualreviews.org
Access provided by Kansas State University on 09/24/18. For personal use only.

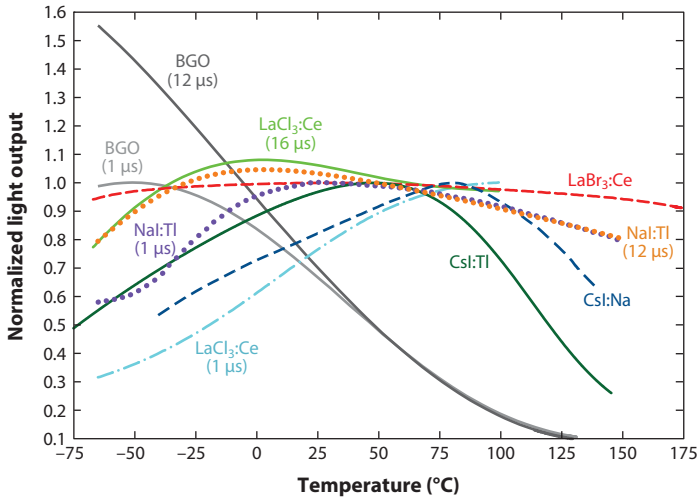

Figure 10

The light output, normalized at the maximum for $\tau = 1$ μs, as a function of temperature for several common inorganic scintillators. The light output data for NaI:Tl, $Bi_4Ge_3O_{12}$ (BGO), and $LaCl_3$ are normalized for data measured with a 1-μs shaping time, and comparison data are provided at longer shaping times. Data are from References 4 and 6.

in $\sigma_e(T)$ with increasing temperature, shown in Equation 3. This increase in $\sigma_e(T)$ spreads the light emission over more wavelengths and reduces the light yield at λ_{max}. Consequently, photon reabsorption with defects increases along with losses from increased wavelength mismatch with the light sensor.

There is a notable decrease in light yield for many scintillators at low temperatures, particularly below room temperature; this decrease is believed to be a consequence of lengthening the primary decay constant. If the time constant of a light sensor is not lengthened to match the relative increase in τ, then an increased number of luminescent photons is not recorded. As **Figure 10** shows, the light output of many common scintillators appears to decrease with lower temperature; however, changing the integration time of the light-sensing system works to include previously lost photons, thereby increasing the relative light yield. Examples of such scintillators include BGO, NaI:Tl, and $LaCl_3$:Ce. Scintillators with relatively flat thermal response over a broad range of energies include $LaBr_3$:Ce and BaF_2 (220-nm emission).

3.7. Fracture Resistance

Fracture resistance is a measure of a scintillation crystal's ability to withstand shock. Many of the alkali-metal halide and lanthanide halide scintillators are soft and extremely fragile and crack under modest exposure to shock. For instance, both NaI and CsI are listed as 2 on the Moh hardness scale,[2] an indicator of resistance to fracture and plastic deformation. NaI is fragile and cracks easily, while CsI is pliable and can withstand more shock. Packaging improvements, which have internal shock resistant buffer regions, have allowed many of these delicate crystals to be

[2]This hardness scale, still used today, was initially developed in 1812 by Friedrich Moh, who compared materials to ten commonly available minerals used as standards. The scale ranges from 1 to 10, with talc rated as 1 and diamond as 10. This scale is neither linear nor logarithmic but is ordinal and somewhat arbitrary in designation.

used in rough environments such as oil well logging. Oxide-based scintillators tend to be more resilient to shock than are alkali halides and offer a solution for measurements conducted in rough environments. Some oxide-based scintillators, such as $Y_3Al_5O_{12}$ (YAG) (8.5) and $YAlO_3$ (YAP) (8.6), have high Moh hardness values.

3.8. Moisture Resistance

Many of the alkali-metal halide and lanthanide halide scintillators are chemically unstable in a humid environment and require handling in special dry rooms during the cutting and packaging process. Furthermore, these hygroscopic crystals must be hermetically sealed in airtight containers to prevent decomposition. Otherwise they may absorb water moisture, which causes them to change color and/or decompose. The alkali-metal halides NaI:Tl and LiI:Tl are very hygroscopic and are ruined if exposed to humidity. The same is true for the lanthanide halides $LaBr_3$:Ce, $LaCl_3$:Ce, and $CeBr_3$. CsI:Na is also hygroscopic; however, pure CsI and CsI:Tl are only slightly hygroscopic. Oxide-based scintillators, along with the alkali-earth halides, are generally not hygroscopic.

3.9. Optical Clarity and Index of Refraction

Scintillators should be transparent to luminescent photons; otherwise they are reabsorbed and undetectable. The optical attenuation coefficient is defined as the distance that a packet of photons reaches with an absorption loss of $1-e^{-1}$ (63.21%). A large Stokes shift assists in optical clarity. The index of refraction is the ratio of light speed in vacuum to light speed in the medium ($n = c/v$). This ratio changes with light wavelength; hence the important value is the index of refraction at the most probable emission wavelength λ_{max}. This index of refraction n should be close to that of the light-sensing instrument for good coupling and light transmission. For typical glass windows, $n \leq 1.5$ is best. For a scintillation crystal placed directly upon the light sensor surface, there is an air gap ($n = 1$) between the two surfaces. A thin layer of optical coupling compound, usually with $1.4 \leq n \leq 1.5$, is applied between the surfaces to eliminate the air gap. For severely mismatched indices of refraction, the coupling compound refractive index should be the geometric mean of the two materials.

3.10. Radiation Absorption Efficiency

The radiation absorption efficiency is a strong function of the atomic number and material density. For gamma-ray detection, the three most important radiation interactions are photoelectric absorption, Compton scattering, and pair production. For these three interactions, high Z values produce more efficient results than do low Z values. Some materials may have one moderately high-Z element and other low-Z elements. Yet the concentration of high-Z elements largely determines the absorption coefficient.

The exponential attenuation of uncollided gamma rays entering a scintillating crystal is given by

$$I(x) = I_o e^{-\mu_t(E)x}, \qquad 15.$$

where I_o is the initial gamma-ray intensity intersecting the material surface and x is the distance into the crystal material. The total interaction coefficient is given by

$$\mu_t(E) = \sum \mu_i(E) \approx \mu_{pe} + \mu_{cs} + \mu_{pp}, \qquad 16.$$

Annu. Rev. Mater. Res. 2018.48:245-277. Downloaded from www.annualreviews.org
Access provided by Kansas State University on 09/24/18. For personal use only.

Annu. Rev. Mater. Res. 2018.48:245-277. Downloaded from www.annualreviews.org
Access provided by Kansas State University on 09/24/18. For personal use only.

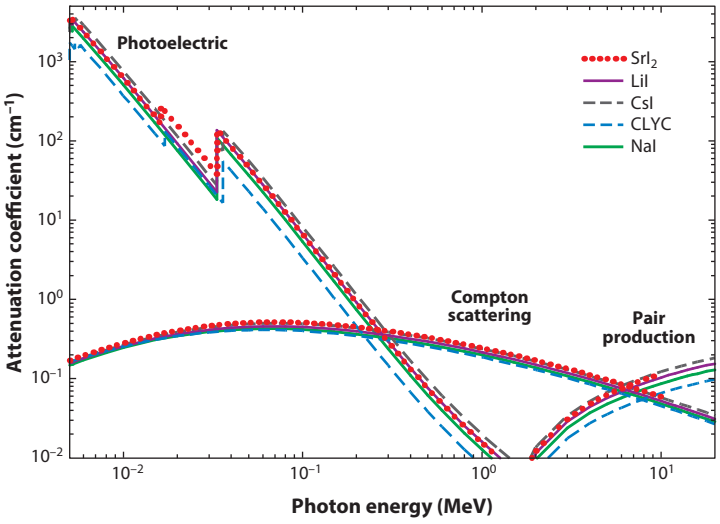

Figure 11

Gamma-ray linear attenuation coefficients for some common alkali-halide and elpasolite scintillators relative to NaI. Abbreviation: CLYC, Cs_2LiYCl_6. Data are from Reference 39.

where the subscripts pe, cs, and pp refer to photoelectric, Compton scattering, and pair production, respectively. Other gamma-ray interactions are possible but are less important to general gamma-ray detection. In the detector community, the ratio $I(x)/I_o$ is termed the interaction efficiency and is the probability that a photon interacts in some manner in the material while traveling a distance x in it. The interaction coefficients for numerous popular inorganic scintillators are graphed in **Figures 11**, **12**, and **13**. In **Figures 11–13**, the interaction coefficients are separated into the contributions from photoelectric, Compton scattering, and pair production.

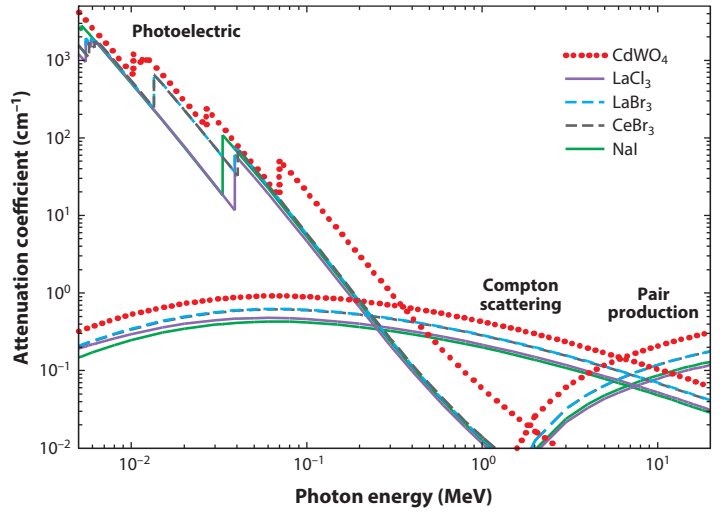

Figure 12

Gamma-ray linear attenuation coefficients for some common scintillators relative to NaI. Data are from Reference 39.

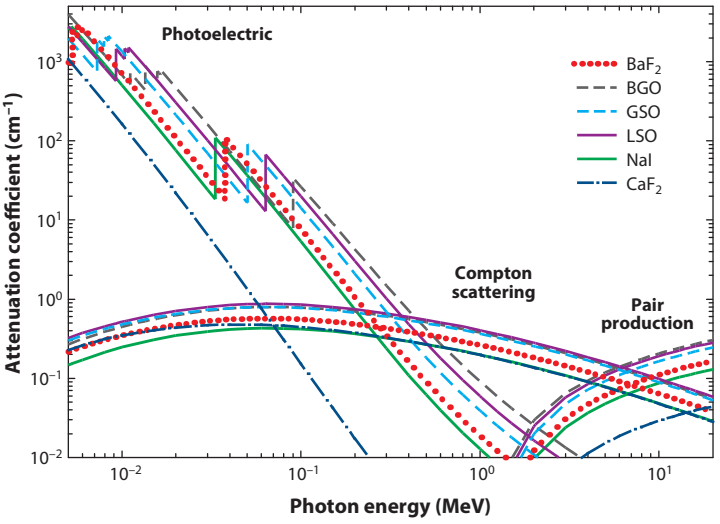

Figure 13

Gamma-ray linear attenuation coefficients for some common scintillators relative to NaI. Data are from Reference 39. Abbreviations: BGO, $Bi_4Ge_3O_{12}$; GSO, Gd_2SiO_5; LSO, Lu_2SiO_5.

The interaction efficiency describes the probability of an interaction, and not the amount of energy absorbed. While photoelectric interactions result in complete photon energy absorption, Compton scattering physically cannot. Usually, multiple Compton scatters and eventual photoelectric absorption must occur for full energy absorption of photons above where $\mu_{pe} \approx \mu_{cs}$. Pair production results in the eventual emission of two 511-keV photons, which may escape the detector. Hence, the absorption efficiency describes the probability of a photon interaction, and not the probability that gamma rays are fully absorbed.

4. SCINTILLATOR MATERIALS FOR GAMMA-RAY SPECTROSCOPY

After more than 120 years of exploration for different scintillators, several hundreds have been identified. For example, tables of scintillators numbering in the hundreds, still incomplete, can be found in the literature (40, 41). It is beyond the scope of the present text to be all inclusive of this extensive list of scintillators, and the author limits the following descriptions to those scintillators that have either proven applications or historical significance or that show potential as scintillators for new applications. For the sake of brevity, information already outlined in **Table 1** is not repeated in the following sections. However, some discussion on the special properties of some interesting and common scintillators follows.

4.1. Alkali-Metal Halides

The alkali-metal halides are scintillators consisting of one element from Group 1 (or group I) and another element from Group 17 (or group VII) in the periodic chart of elements. Scintillators of this type were some of the first bright inorganic scintillators to be discovered, including NaI:Tl.

4.1.1. Sodium iodide (NaI, NaI:Tl). The most widely used inorganic scintillator is NaI:Tl. The notation :Tl indicates that the NaI crystal has been doped with the activator Tl. It is one of the

Annu. Rev. Mater. Res. 2018.48:245-277. Downloaded from www.annualreviews.org
Access provided by Kansas State University on 09/24/18. For personal use only.

brightest scintillators available, has acceptably good light yield proportionality, and can be grown in large sections. NaI:Tl was first reported by Hofstadter (42), who initially prepared a powder sample of material with thallium added to the mixture that produced scintillation light when exposed to alpha particles. The sample was found to be hygroscopic, turning yellow within a few hours when exposed to room air. He then produced tiny NaI:Tl crystals (approximately 1–2 mm in size) in an evacuated ampoule. These crystals proved to be brighter than other scintillating materials known at the time.

The emission spectrum from NaI:Tl matches well to the spectra of common K-bialkali and S-11 commercial PMTs. NaI:Tl shows nonproportional light yield in the low-energy region, below 200 keV, which consequently compromises spectroscopic performance. Regardless, NaI:Tl performs adequately well as a general-use gamma-ray spectrometer. The relatively long decay time generally precludes it from being a candidate for fast timing measurements.

NaI:Tl has a slow 150-ms phosphorescent component, contributing approximately 9% of the photoelectron yield (43). The emission rate is relatively low but usually does not interfere with low activity measurements, mainly because the low emission rate of phosphorescence produces low-pulse-height events easily rejected by a discriminator. This phosphorescent yield becomes important for high gamma-ray interaction rates, during which it can become a steady source of background noise termed afterglow.

NaI:Tl is available in many different sizes, ranging from cylinders that are only 0.5 inches in diameter to sheets almost a meter in diameter. The most preferred radiation detector geometry remains the 3 × 3 inch right circular cylinder. It is the most characterized NaI:Tl detector size with extensive efficiency data in the literature. Furthermore, it is the standard by which all other inorganic scintillators are measured.

NaI:Tl is widely used to measure X-rays and gamma rays because of its high efficiency for electromagnetic radiation, mainly due to the high interaction efficiency of iodine. NaI:Tl detectors do not require cooling during operation and can be used in a great variety of applications. The bare NaI:Tl crystal is hygroscopic and fragile. However, when NaI:Tl crystals are properly packaged in ruggedized containers, field applications are possible, and NaI:Tl detectors can operate over a long time period in warm and humid environments, resist a reasonable level of mechanical shock, and are resistant to radiation damage.

Pure NaI also produces scintillation light without the assistance of activator dopants. At room temperature, the light yield of pure NaI is low, having less than 2% energy conversion efficiency with a most probable emission wavelength of λ_{max} around 310 nm (44, 45). Measurements by Moszyński et al. (46) at room temperature show a release of 1,000 photoelectrons/MeV for a bialkali-type PMT (47). The decay constant is substantially smaller for pure NaI than for NaI:Tl, being less than 20 ns at room temperature. At cryogenic temperatures, the light yield increases tremendously up to 25% energy conversion efficiency, a yield of between 44,000 and 63,000 photons per megaelectron volt with a maximum light emission at approximately 77 K (45, 48). This trend of increased light yield with reduced temperature is observed for the entire family of pure alkali-metal/iodine scintillators (49).

Problems with operating scintillators coupled to PMTs at low temperature (45) include inefficient cooling of the PMT, property changes in coupling compounds at cryogenic temperatures, and scintillator self-absorption losses. At least one of these problems is addressed by coupling pure NaI to a photodiode instead of attaching the crystal to a PMT (47, 48).

4.1.2. Cesium iodide (CsI, CsI:Tl, CsI:Na). CsI:Tl is slightly hygroscopic and is much more resilient than NaI:Tl. CsI:Tl can be machined (to some extent), and it has significantly fewer problems with shock and fracturing. Thin sheets of CsI:Tl are slightly malleable and can be

Annu. Rev. Mater. Res. 2018.48:245-277. Downloaded from www.annualreviews.org
Access provided by Kansas State University on 09/24/18. For personal use only.

formed over curved surfaces. With constituent elements Cs ($Z = 55$) and I ($Z = 53$), the gamma-ray attenuation coefficient is higher than that of NaI:Tl (see **Figure 11**), and the gamma-ray intrinsic detection efficiency per unit volume is higher than that of NaI:Tl.

Although CsI:Tl has a considerably higher light yield relative to most inorganic scintillators, the large mismatch of the luminescent spectrum with the response functions of common PMTs compromises the spectroscopic performance. Long shaping times can improve performance by collecting more of the scintillation photons, but at the expense of more electronic noise. The maximum emission wavelength matches well to the response function of Si photodiodes (SiPDs), and reasonable spectroscopic performance is realized with SiPDs or SiPMs. The maximum light output of CsI:Tl is observed at approximately 50°C and reduces with lower or higher temperatures (**Figure 10**), where ±50°C from the optimum causes a reduction of >15%. Light loss to gamma radiation damage can become significant at doses approaching 10 gray, with a measured light reduction of 15% (6). Pure CsI and CsI:Tl recover from radiation damage at room temperature, but at a rate of less than 0.5% per day. Thermal annealing of CsI or CsI:Tl does not assist with recovery and appears to make matters worse if conducted at temperatures exceeding 300°C.

Thick layers (2 mm) of CsI:Tl grown by physical vapor deposition form narrow, vertical, crystalline columns (50, 51) that perform as miniature optical fibers. The CsI:Tl thin film can be patterned through optical lithography methods to place the scintillator on select locations (50). When coupled to a SiPD or SiPM, the structure can be used to image a collimated beam of X-rays.

A variant of CsI has Na as the activation dopant but is much more hygroscopic than CsI:Tl. The luminescent spectrum from CsI:Na is a better match to common K-bialkali and S-11 PMTs (**Figure 3**), approximately 85% of that observed with NaI:Tl (6). However, the longer decay times and the lower-resolution performance offer little advantage over NaI:Tl. The maximum light output of CsI:Na is observed at approximately 80°C. Temperature deviation of ±50°C from the optimum causes a light yield reduction of >20%.

Undoped CsI also produces scintillation light, with λ_{max} at 315 nm (6). Amsler et al. (52) report the existence of three decay constants all significantly shorter than activated CsI, namely 28 ± 2 ns, 6 ± 1 ns, and a third fast component reported to be 2 ns. The light yield of pure CsI increases significantly at low temperature, with light yield of 50,000 ± 5,000 photons per megaelectron volt at 77 K (52) and energy resolution of 8.3% FWHM for 511-keV photons. Only a single decay constant was observed at low temperatures, which increased significantly up to approximately 1 μs at 85 K.

4.1.3. Lithium iodide (LiI:Eu). Lithium iodide (LiI) can be used for gamma-ray and neutron detection. LiI is hygroscopic and requires that all handling be performed in a dry environment. LiI activated with Eu (LiI:Eu) remains the most studied and used of the LiI variants. With a mass density of 4.08 g/cm^3, LiI:Eu has nearly the same gamma-ray interaction efficiency as does NaI:Tl. Two decay constants are observed: one at 185 ns yielding 88% of the photons and a slower decay time at 1.089 μs yielding the remaining 12% of photons (53). The longer maximum wavelength of LiI:Eu causes mismatch with standard PMTs. The Li constituent of LiF:Eu enables thermal-neutron detection through the ^{6}Li(n,^{3}H)^{4}He reaction. If the Li is replaced with enriched ^{6}Li, the thermal-neutron absorption macroscopic cross section can be increased to 17.27 cm^{-1}, and the absorption length reduces to 0.58 mm.

4.1.4. Some other alkali-metal halide scintillators. Potassium iodide (KI) was investigated by Hofstadter (42) before NaI and led to the investigation of NaI:Tl powders as a scintillator. KI:Tl has a light yield of approximately 9,700 photons/MeV (14) and two main decay branches at 240 ns and 2.5 μs (54). There is evidence of different decay constants of 210 ns and 1.76 μs when KI:Tl

Annu. Rev. Mater. Res. 2018.48:245-277. Downloaded from www.annualreviews.org
Access provided by Kansas State University on 09/24/18. For personal use only.

is irradiated with alpha particles instead of gamma rays. The emission spectrum has a reported maximum between 400 nm and 425 nm (55, 59, 60). KI has a density of 3.12 g/cm^3, which is lower than that of NaI, and an index of refraction of 1.68. Natural potassium has a radioactive isotope, ^{40}K, that produces an intrinsic radiation background with K-based scintillators.

Cesium fluoride (CsF) is a fast inorganic scintillator initially studied by Van Sciver & Hofstadter (56). It has a mass density of 4.12 g/cm^{-3} and is hygroscopic. CsF scintillates without the assistance of an activator dopant, with $\lambda_{max} = 390$ nm (57). The absolute photon yield is approximately 1,950 photons/MeV at room temperature (57, 58). CsF has an index of refraction of 1.48, below that of common glass. The measured decay time is 5 ± 1 ns, making CsF one of the fastest inorganic scintillators available.

Cesium bromide (CsBr) is a heavy element alkali-metal halide with a density of 4.44 g/cm^3 and refractive index of 1.7. It is also hygroscopic, like many alkali-metal halides. CsBr activated with Tl has two main decay times that differ with the type of radiation particle (54, 61). Notably, alpha particles (5.3 MeV) were observed to produce shorter decay times at 2.3 ± 0.15 μs and 14.5 ± 1.34 μs relative to electrons (from 662-keV gamma rays) at 2.57 ± 0.13 μs and 24.23 ± 1.5 μs (61). Pure CsBr also scintillates, reportedly only 20 photons/MeV (58). The decay constant of pure CsBr is unusually short for an alkali-metal halide at 0.07 ns, with $\lambda_{max} = 250$ nm.

4.2. Alkali-Earth Halides

For each molecule, the alkali-earth halide scintillators generally have at least one atom from Group 2 (group II) and two atoms from Group 17 (group VII) in the periodic chart of elements. Many of these scintillators are exceptionally bright, and a few are described in the following subsections.

4.2.1. Barium fluoride (BaF_2). Barium fluoride (BaF_2) is relatively soft, with a ranking of 3 on the Moh hardness scale, and it has two intrinsic luminescent emissions. Although not as bright as the longer wavelength emission, BaF_2 is mainly important for its fast decay time at the 220-nm emission (62). The absorption of light in common soda-lime glass is too high to allow transmission for luminescent wavelengths. Instead, a PMT with a fused quartz window is preferred if the 220-nm wavelength is to be used. The predicted and measured radiation hardness of BaF_2 is relatively high (62–66), with exposures up to 1.3×10^7 rad having minimal loss of only 1% cm^{-1} light transmission. BaF_2 crystals have shown good resistance to gamma-ray irradiation up to 10^6 rad. Another study showed that Pb contaminants in BaF_2 significantly reduced radiation hardness (67).

An interesting physical aspect to the light emissions from BaF_2 is that the 310-nm emission is greatly affected by temperature changes while the 220-nm emission is not (68). The 310-nm emission spectrum increases, by three times, its room temperature output when reduced to 175 K and practically disappears at temperatures above 358 K. The 220-nm emission is unaffected by these temperature changes.

4.2.2. Calcium fluoride (CaF_2:Eu). Europium-activated calcium fluoride is a commercially available scintillator that is not hygroscopic and is practically insoluble in water. It has a ranking of 4 on the Moh hardness scale. Because it is not hygroscopic and relatively robust, it can be used under rough circumstances otherwise inappropriate for delicate crystals. The atomic numbers of the elemental constituents are 20 and 9, both relatively low for gamma-ray detection. CaF_2:Eu can be used as a beta particle detector because backscattering is reduced by the low-Z constituents (69). The refractive index at λ_{max} is 1.47 and has minimal internal reflection when coupled to glass windows.

Annu. Rev. Mater. Res. 2018.48:245-277. Downloaded from www.annualreviews.org
Access provided by Kansas State University on 09/24/18. For personal use only.

4.2.3. Calcium iodide (CaI_2). Calcium iodide is a strongly hygroscopic scintillator initially studied by Van Sciver, Hofstadter, and colleagues (23, 24, 70, 71). Europium-activated CaI_2 yielded excellent results, with up to 200% light yield relative to NaI:Tl crystals. Recent work on CaI_2 indicates that the theoretically achievable light yield for CaI_2:Eu is 114,000 photons/MeV, with a measured value of 110,000 photons/MeV (26). CaI_2 has a rhombohedral crystalline lattice formed in a layered structure with weak bonds between the basal planes. Unfortunately, the crystal is prone to cracking and plastic deformation during both crystal growth and detector fabrication, and such defects are most likely the reason why CaI_2 has not been extensively explored. Methods to improve crystal growth and material quality have been implemented (72), although scintillation performance was lower than earlier results reported by Hofstadter (23, 24).

4.2.4. Strontium iodide (SrI_2:Eu). Strontium iodide activated with Eu, initially studied by Hofstadter (73), is a hygroscopic scintillator and has recently regained attention as a potential high-resolution scintillator. The high density of SrI_2 combined with the relatively high Z constituent atoms [38/53] makes SrI_2 an efficient gamma-ray absorber (see **Figure 11**). SrI_2:Eu has a relatively long decay time, which makes it less attractive than NaI:Tl and $LaBr_3$:Ce for high-count-rate applications. The relative light yield is good with a nominally proportional response down to 15 keV (see **Figure 8**), which increases at low temperature (80 K) and decreases significantly at temperatures above 300 K (74). Spectral broadening of the emission and an increase in decay constant τ were observed as temperature was increased from 100 K to 600 K (74). This increase in τ with temperature is hypothesized to be from photon self-absorption. Pure SrI_2 also scintillates, but these scintillations appear to be defect related because defect-free crystals do not demonstrate this property (75).

4.3. Lanthanide Halides

The family of lanthanide halide scintillators, consisting of one lanthanide element and three of an element from Group 17, are some of the brightest scintillators discovered thus far.

4.3.1. Cerium bromide ($CeBr_3$). Although cerium bromide ($CeBr_3$) was synthesized as early as 1899 (76), only recently was it recognized as a bright scintillator (29). Luminescence from $CeBr_3$ arises from an excited state of the Ce^{3+} and does not require an activator dopant. A moderately heavy element scintillator, $CeBr_3$ has good gamma-ray absorption efficiency (see **Figure 12**). $CeBr_3$ has a hexagonal crystal structure and is hygroscopic and fragile, easily cleaving along the slip planes (77). Methods have been implemented to reduce the fragility of $CeBr_3$ and other lanthanide halides, using aliovalent doping to inhibit cracking (78). Tests with gamma-ray irradiation indicate that $CeBr_3$ can withstand doses exceeding 100 kGy with only a minor decrease in energy resolution (31). $CeBr_3$ has a relatively linear light yield, allowing for good energy resolution. For example, 3.2% FWHM energy resolution was reported for 662-keV gamma rays (79).

4.3.2. Lanthanum chloride ($LaCl_3$:Ce). Introduced in 2001 (80), Ce-activated lanthanum chloride ($LaCl_3$:Ce) is a bright and fast scintillator with a relatively linear light yield (**Figure 8**). The gamma-ray detection efficiency is similar to that of NaI:Tl. The material is very hygroscopic and brittle and has a hexagonal crystal structure that cleaves easily along the {100} planes. The most probable emission wavelength is not well matched to the response function of common PMTs. The absolute light yield is higher than that of NaI:Tl, but because of the spectral mismatch, its signal response is less than that of NaI:Tl. Commonly reported energy resolution is near 4.0% FWHM at 662 keV for various crystal sizes. The light yield from $LaCl_3$:Ce decreases with decreasing temperature; however, if the integration time constant is increased, the light output response is fairly constant over a wide temperature range (**Figure 10**).

Annu. Rev. Mater. Res. 2018.48:245-277. Downloaded from www.annualreviews.org
Access provided by Kansas State University on 09/24/18. For personal use only.

4.3.3. Lanthanum bromide ($LaBr_3$:Ce). Ce-activated lanthanum bromide ($LaBr_3$) was introduced in 2002 (81). Due to its relatively high *Z* elements and mass density, it has good gamma-ray absorption efficiency (see **Figure 12**). The material is very hygroscopic and brittle and has a hexagonal crystal structure that cleaves easily along the {100} planes. The PMT output is between 130% and 165% relative to NaI:Tl. The emission spectra match well enough with the response function of common PMTs to produce high energy resolution with reported values below 2.9% FWHM at 662 keV for various crystal sizes. The excellent energy resolution is a combined effect of the absolute light yield and the good relative light yield proportionality. $LaBr_3$ is also a relatively fast scintillator (see **Table 1**).

4.4. Transition Metal Scintillators

There are many scintillators that are minerals composed of at least one or more transition metal elements. These scintillators include perovskites and garnets, a few of which are described in the following subsections.

4.4.1. Yttrium aluminum perovskite ($YAlO_3$:Ce or YAP:Ce). Yttrium aluminum oxide ($YAlO_3$ or YAP) is a perovskite[3] scintillator. Perhaps the most interesting property of YAP:Ce is its unusually good linearity in the low-energy range, leading to energy resolution approaching the theoretical maximum. For example, a FWHM of 4.4% was reported for ^{137}Cs 662-keV gamma rays (12, 47). Other advantages of YAP:Ce include a fast decay time, relatively high mechanical strength, and chemical and thermal stability (28). Disadvantages include low-*Z* constituent elements, a high index of refraction, and a relatively low value of λ_{max}. The low value of λ_{max} causes inefficient coupling with common PMTs.

4.4.2. Lutetium aluminum perovskite ($LuAlO_3$:Ce or LuAP:Ce). Lutetium aluminum oxide ($LuAlO_3$ or LuAP), also a rare-earth perovskite, has many similar properties as YAP. The most important differences are the higher density of 8.34 g/cm^3 and higher-*Z* constituents of LuAP, yielding one of the highest gamma-ray attenuation coefficients for scintillators. It is also a fast-decay scintillator. Both the light yield and λ_{max} are relatively low, and *n* is high. Consequently, these disadvantages yield lower energy resolution of LuAP:Ce relative to YAP:Ce (82). Although the light yield of LuAP:Ce is only 26.5% of that of NaI:Tl, the energy resolution of LuAP:Ce is comparable to that of NaI:Tl, primarily due to the good light yield proportionality (82).

4.4.3. Yttrium aluminum garnet ($Y_3Al_5O_{12}$:Ce or YAG:Ce). Ce-activated yttrium aluminum garnet[4] ($Y_3Al_5O_{12}$:Ce or YAG:Ce) is a nonhygroscopic, relatively fast, inorganic scintillator that has found use with scanning electron microscope (SEM) systems (83, 84). It rates 8.5 on the Moh hardness scale and has relatively high resistance to radiation damage, making it suitable for use under the expected high electron bombardment in a SEM. The emission wavelength is high, and extended red PMTs are recommended. SiPDs are also good alternatives. The absolute light yield is higher when measured with a SiPD than with a PMT (85). Depending on the doping concentration and type of radiation, YAG:Ce has multiple decay times (86) and can be used to identify radiation types through pulse shape discrimination (85).

4.4.4. Lutetium aluminum garnet ($Lu_3Al_5O_{12}$ or LuAG). The higher-*Z* component of lutetium makes lutetium aluminum garnet ($Lu_3Al_5O_{12}$ or LuAG) an interesting material for

[3] Discovered in the Ural Mountains in 1839 by Gustav Rose, this mineral is named after the Russian mineralogist Lev Perovski.

[4] The word garnet is derived from the Middle English word gernet, which means dark red.

Annu. Rev. Mater. Res. 2018.48:245-277. Downloaded from www.annualreviews.org
Access provided by Kansas State University on 09/24/18. For personal use only.

gamma-ray detection. A comprehensive review by Nikl et al. (32) provides general information on its development. LuAG is a nonhygroscopic cubic crystal of 8.5 on the Moh hardness scale. LuAg yields good performance with Ce (87) and Pr (88) activator dopants, with light yield up to 22,000 photons/MeV for commercial material (89). Furthermore, LuAg is a relatively fast scintillator. The light yield proportionality is quite excellent for energies above 100 keV (16) and assists with the good energy resolution observed, with the best resolution reported as 4.2% at 662 keV for commercial LuAG:Pr.

4.4.5. Zinc sulfide (ZnS:Ag). Discovered in 1866 by Théodore Sidot, zinc sulfide (ZnS) is a mature, nonhygroscopic scintillator. It is relatively bright for heavy charged particles but inefficient as a gamma-ray detector, a feature used as a natural discrimination tool for particle detection. Its dual crystallinity leads to polymorphism, and consequently ZnS is usually acquired as polycrystalline powder or as thin optical crystals. ZnS is also a wide-band-gap semiconductor material, with its hexagonal and cubic forms having band gaps of 3.91 eV and 3.54 eV, respectively. Ag-doped ZnS (ZnS:Ag) in the form of polycrystalline powder is opaque to its own light emissions for mass thicknesses greater than 25 mg/cm^2 (or 61 μm). Hence, most detectors utilizing ZnS:Ag are limited to thin films.

4.5. Post–Transition Metal Scintillators

There are a few scintillators composed of elements following the transition elements, mainly from Groups 13 through 16. Of these, only one relatively important scintillator, bismuth germanate ($Bi_4Ge_3O_{12}$ or BGO), is discussed in the present work.

4.5.1. Bismuth germanate ($Bi_4Ge_3O_{12}$ or BGO). BGO is a relatively rugged, fracture-resistant, nonhygroscopic material, and it is rated as 5 on the Moh hardness scale. BGO has one high-Z constituent, along with relatively high density of 7.13 g/cm^3, making it a good gamma-ray absorber (see **Figure 13**), and it has found practical use in the medical imaging industry (90). Ishii & Kobayashi (62) report that it is a relatively radiation hard material capable of withstanding gamma-ray doses between 10^4 and 10^5 rad before showing significant light absorbance. The combination of high refractive index and low light yield produces lower energy resolution for BGO than for NaI:Tl, approximately 15% FWHM for 662-keV gamma rays (91). BGO also has a fast-decay component, not listed in **Table 1**, of 60 ns with lower photon yield (700 photons/MeV). BGO scintillates without an activator, the luminescence caused by intrinsic $^3p_1 \rightarrow {}^1s_0$ transitions of the Bi^{3+} ions in the crystals (92). BGO light yield is strongly dependent upon temperature and shows high thermal quenching above room temperature. Provided that an adequately long electronic shaping time is applied, the absolute light yield of BGO at 77 K can be double its room temperature yield (see **Figure 10**).

4.6. Rare-Earth Oxyorthosilicates

There are numerous promising scintillators composed of rare-earth minerals, silicon, and oxygen, named the rare-earth oxyorthosilicates. Some of these interesting scintillators are now being used for special applications in radiation detection.

4.6.1. Gadolinium oxyorthosilicate (Gd_2SiO_5:Ce or GSO:Ce). Ce-doped gadolinium oxyorthosilicate (Gd_2SiO_5 or GSO) has one high-Z constituent and relatively high density and is thus a good absorber of gamma rays. GSO is monoclinic and is not hygroscopic. It has two decay components when doped with the activator Ce. Energy resolution of less than 7.0% FWHM at

Annu. Rev. Mater. Res. 2018.48:245-277. Downloaded from www.annualreviews.org
Access provided by Kansas State University on 09/24/18. For personal use only.

662 keV has been reported (93, 94), with further improvement accomplished with highly purified materials (94) and codoped materials (95). GSO is also a thermally stable scintillator and has been used for oil well logging (96). Due to GSO's good gamma-ray detection efficiency and superior energy resolution relative to BGO, GSO has been used as a replacement in medical imaging instruments (97). Studies show that GSO is nonproportional over a wide energy range (98) but has better proportionality than either lutetium oxyorthosilicate (Lu_2SiO_5 or LSO) or yttrium oxyorthosilicate (Y_2SiO_5 or YSO). GSO has a natural radioactive background component from ^{152}Gd, which has a natural abundance of 0.2% and emits 2.14-MeV alpha particles. With the large thermal-neutron reaction cross section of natural gadolinium (49,000 barns, where a barn is an interaction cross-section unit equal to 10^{-24} cm^2), GSO has been studied as a possible neutron detector by way of prompt neutron reactions in Gd (99), relying upon the detection of conversion electrons and gamma-ray emissions from neutron absorptions. GSO is sensitive to background radiations that can be falsely interpreted as neutron-induced events.

4.6.2. Lutetium oxyorthosilicate (Lu_2SiO_5:Ce or LSO). Discovered and developed by Melcher in 1990 (see References 100–103), Ce-activated LSO was originally developed for oil well logging but is precluded from this application because performance severely degrades at the elevated temperatures. The crystal is robust and nonhygroscopic and is rated as 5.8 on the Moh hardness scale. Both the absolute light yield and mass density are higher than those of BGO (103), and with its high-*Z*-number constituent Lu, it has excellent gamma-ray absorption efficiency (see **Figure 13**). The energy resolution of LSO:Ce is also lower than that of NaI:Tl, but at 10.3% FWHM at 662 keV, the energy resolution of LSO is much better than that of BGO. Furthermore, LSO is radiation hard, with a reported radiation limit of greater than 10^6 rad. It also has relatively proportional light yield for gamma-ray energies above 200 keV but not below 100 keV. A significant problem with LSO:Ce is that it is naturally radioactive from ^{176}Lu (2.59% isotopic abundance), which emits beta particles and gamma rays. This problem is further exacerbated by unintentional doping with other radioactive impurities from the crystal growth source materials. LSO:Ce also has long phosphorescence, which has been measured to last several seconds (104). Nassalski et al. (105) generally conclude that the long phosphorescence precludes LSO:Ce from applications in CT systems. However, for specific applications such as PET measurements, which use coincidence counting, this natural background is of less concern. Due to these beneficial properties of LSO, it is now replacing BGO in modern PET scan imaging systems.

4.6.3. Yttrium oxyorthosilicate (Y_2SiO_5:Ce or YSO:Ce). Ce-activated YSO (YSO:Ce) is a nonhygroscopic rare-earth oxyorthosilicate. YSO is disadvantaged as a gamma-ray spectrometer due to its relatively low *Z* constituents and moderate mass density. YSO:Ce has good light yield proportionality above 100 keV (106). Commercial YSO:Ce usually has an absolute light yield around 10,000 photons/MeV (93), although a higher light yield of approximately 24,000 photons/MeV has been reported for optimized crystals (98, 106). Codoping with Ce/Ca has a reportedly small effect, with a resulting absolute light yield of 21,200 photons/MeV. The usual reported energy resolution is 9–9.4% FWHM for 662-keV gamma rays, although energy resolution as low as 7.4% FWHM has been reported (107).

4.6.4. Lutetium yttrium oxyorthosilicate ($Lu_{1.8}Y_{0.2}SiO_2$:Ce or LYSO:Ce). Ce-activated lutetium yttrium oxyorthosilicate ($Lu_{1.8}Y_{0.2}SiO_2$:Ce or LYSO:Ce) was developed to include the advantages of LSO and YSO (108–110). LYSO:Ce is commercially available, with similar properties as LSO:Ce (111, 112). LYSO:Ce has similar radiation hardness as LSO, but it produces increased afterglow phosphorescence with radiation damage. LYSO:Ce is robust and nonhygroscopic with a Moh hardness of 5.8. Energy resolution is similar to LSO, near 10% FWHM for

Annu. Rev. Mater. Res. 2018.48:245-277. Downloaded from www.annualreviews.org
Access provided by Kansas State University on 09/24/18. For personal use only.

662 keV (110). Because of the natural abundance of ^{176}Lu, LYSO:Ce has an intrinsic radioactive background. Cooke et al. (108) report a lower temperature dependence on light yield than observed with LSO. Advantages of LYSO over LSO include lower production costs, fewer defects, and easier incorporation of the Ce activator into the crystal lattice (108).

4.7. Elpasolites

The general formula for an elpasolite[5] is K_2NaAlF_6. Many recently developed Ce-activated elpasolites have light yield similar to that of NaI:Tl. A unique property of several elpasolite scintillators with Li substituted for Na is that they have dual use as gamma-ray and neutron detectors.

4.7.1. Cesium lithium yttrium chloride (Cs_2LiYCl_6:Ce or CLYC:Ce). Ce-doped cesium lithium yttrium chloride (Cs_2LiYCl_6:Ce or CLYC:Ce) is an elpasolite dual-use inorganic scintillator that can detect both gamma rays and neutrons. CLYC:Ce is hygroscopic and must be encapsulated. The luminescent emissions for CLYC:Ce are centered at 372 nm and 400 nm, while undoped CLYC has a single emission centered at 305 nm (33). Despite the low light yield and long decay constants of CLYC:Ce, good energy resolution has been reported: 4.2% FWHM for 662-keV gamma rays (113). The Li constituent of CLYC:Ce allows for neutron detection. For natural Li as a constituent, the macroscopic cross section for the ^{6}Li(n,^{3}H)^{4}He reaction is 0.248 cm^{-1}, yielding an absorption length of 4 cm. If enriched ^{6}Li is used, the thermal-neutron macroscopic absorption cross section increases to 3.27 cm^{-1}, and the absorption length is reduced to 3 mm. There is also a core valence emission, with a decay constant of 2 ns with a yield of 660 photons/MeV (no Ce doping) to 0 photons/MeV (3% Ce doping) (114). This core valence emission appears under gamma-ray irradiation, but not under alpha particle irradiation. Detection of this emission can be used to distinguish between gamma-ray and neutron-induced heavy charged particle emissions. Because of competing absorptions from ^{35}Cl, CLYC is limited to ~80% thermal-neutron detection efficiency.

4.7.2. Cesium lithium lanthanum bromide ($Cs_2LiLaBr_6$:Ce or CLLB:Ce). Ce-doped cesium lithium lanthanum bromide ($Cs_2LiLaBr_6$:Ce or CLLB:Ce) has dual use as a gamma-ray and neutron detector. CLLB:Ce has multiple decay constants reportedly at 180 ns and 1,100 ns (6), and there is no reported core valence emission for CLLB. The luminescent emissions for CLLB:Ce are centered at 390 nm and 420 nm (115, 116). With Ce doping, the luminescent yield is between 43,000 photons/MeV and 60,000 photons/MeV (6, 115, 117). This high light output, along with the fact that the luminescent yield is more proportional than that found with CLYC:Ce, indicates that CLLB:Ce is a promising new scintillator. Energy resolution of ~3.0% FWHM for 662-keV gamma rays has been reported (115, 117). The Li constituent of CLLB:Ce enables neutron detection. The substitution of Br for Cl reduces neutron losses, while the substitution of La for Y slightly increases neutron losses. With enriched ^{6}Li, the thermal-neutron macroscopic absorption cross section is 2.67 cm^{-1}, with an absorption length of 3.75 mm. Commercial CLLB scintillation detectors have recently become available (6).

4.7.3. Other notable elpasolites. Other promising bright elpasolite scintillators include Cs_2NaLaI_6:Ce, $Cs_2LiLaCl_6$:Ce, $Cs_2NaLaBr_6$:Ce, and Cs_2LiLaI_6:Ce. These scintillators are

[5]The etymology of this term comes from the location where these minerals were discovered: El Paso County, Colorado, USA.

Annu. Rev. Mater. Res. 2018.48:245-277. Downloaded from www.annualreviews.org
Access provided by Kansas State University on 09/24/18. For personal use only.

relatively proportional, provide good light yield, and have short decay constants (~50 ns) (118). Kerisit et al. (119) report that elpasolites substituting Br for Cl should theoretically have higher light yields, and they quote theoretical light yields above 100,000 photons/MeV for $Cs_2LiLaBr_6$:Ce and Cs_2LiYBr_6:Ce. Gundiah et al. (120) report a light yield of approximately 46,000 photons/MeV for $Cs_2NaLaBr_6$:Ce, with an energy resolution of 3.9% FWHM at 662 keV. Two emission maxima were observed at 387 nm and 415 nm, both adequately matched to a bialkali PMT. A recent introduction to the elpasolite family that shows great promise is $Cs_2LiLa(Br_{6-x}Cl_x)$:Ce or CLLBC:Ce, which has good gamma-ray energy resolution (~3% FWHM at 662 keV) and retains the neutron detection characteristic of CLYC:Ce (116).

Rb_2LiYBr_6:Ce, and many others, shows bright light output for neutron absorption (121). Rb_2LiYBr_6:Ce produces between 59,000 ± 5,400 and 83,000 ± 8,300 photons per neutron capture, depending on the Ce^{3+} concentration. The light yield for gamma rays ranges between 16,500 ± 1,600 and 23,000 ± 2,300 photons/MeV, respectively, for Ce^{3+} with concentrations in the 0.1–0.5% range. It has at least three main decay components, reported as 71 ns (31%), 400 ns (53%), and 1,400 ns (16%). Energy resolution for 662-keV gamma rays as low as 4.6% FWHM was reported (122). The difference in light output between gamma-ray and neutron interactions, along with good energy resolution, allows for pulse height discrimination between neutron and gamma-ray events.[6]

4.8. Ceramic and Glass Scintillators

Initially developed by GE Corporation (123, 124), ceramic casting is an alternative scintillator production method to single-crystal growth. Advantages include high radiation hardness, low production costs, hardness, machinability, nonhygroscopy, and environmental robustness, and ceramic and glass scintillators can be manufactured in large sizes usually difficult to produce as single crystals. Greskovich & Duclos (125) describe the criteria for starting materials and the general production process. Cubic crystal structure has been identified as a condition for successful production of high-light-yield ceramic scintillators (124). Noncubic crystals have increased refraction at grain boundaries that increase light self-absorption, which in turn decreases light yield.

Among the earliest materials investigated were BaFCl:Eu, LaOBr:Tb, CsI:Tl, $CaWO_4$, and $CdWO_4$ (123). Bixbyite ceramic scintillator structures[7] were investigated by DiBianca et al. (124) and include Gd_2O_3, Y_2O_3, La_2O_3, and Lu_2O_3. Neither Gd_2O_3 nor La_2O_3 is cubic in form, but both are made cubic by incorporating approximately 50 mol% of Y_2O_3 into the ceramic. Both Y_2O_3 and Lu_2O_3 are cubic structured. Lu_2O_3:Eu has been developed for X-ray imaging (126) and has reported properties of 9.4 g/cm^3 mass density, a λ_{max} of 610 nm, a light yield of approximately 60% of that of CsI:Tl, and a long decay time constant τ of 1.3 ms. The production of $(Y,Gd)_2O_3$:Eu ceramic scintillators led to their incorporation into CT scanners (127). The reported properties of $(Y,Gd)_2O_3$:Eu are a λ_{max} of 611 nm, a decay constant τ of 960 μs, and an optical attenuation coefficient of 1 cm^{-1}.

Other ceramics under investigation include garnets, perovskites, bixbyites, and pyrochlores[8] (128). Two interesting ceramic scintillators recently developed are $Gd_{1.5}Y_{1.5}Ga_2Al_3O_{12}$ (GYGAG)

[6]The Q-value for the ^{6}Li(n,^{3}H)^{4}He reaction is 4.7 MeV, giving an upper light yield of approximately 17,300 photons/MeV, similar to that for gamma-ray events. However, gamma rays with energies approaching 4.78 MeV are not likely to be fully absorbed, so discrimination is still possible.

[7]These structures were named after Maynard Bixby, who discovered the ore in 1897.

[8]The etymology comes from the Greek πῦρ (pyr = fire) and χλωρός (chloros = green) because pyrochlores often turn green with a common flame blowpipe analysis.

Annu. Rev. Mater. Res. 2018.48:245-277. Downloaded from www.annualreviews.org
Access provided by Kansas State University on 09/24/18. For personal use only.

and $Gd_{0.3}Lu_{1.6}Eu_{0.1}O_3$ (GLO) (129, 130). GYGAG:Ce is a robust transparent ceramic with mass density of 5.8 g/cm^3 and an absolute light yield of approximately 50,000 photons/MeV and has at least two decay times of 250 ns and 1.7 μs. The slower component is thought to be a consequence of the energy transfer process in the scintillator (131). Energy resolution of 4.5% FWHM at 662 keV has been reported for a GYGAG:Ce/PMT arrangement. Resolution improved when coupled to a SiPD with 3–3.5% FWHM at 662 keV (130). Eu-activated gadolinium lutetium europium oxide (GLO:Eu) is used for megaelectron volt–photon radiography. The material has a high mass density of 9.1 g/cm^3 and an absolute light yield of approximately 55,000 photons/MeV (130).

Ce-activated glass scintillators were originally developed by Corning Glass Company (see Reference 132), with Ce-activated high-silica glass performing the best. Voitovetskii and colleagues (133, 134) reported different compositions of $Li_2O{\cdot}Si_2O$:Ce glass as neutron-detecting scintillators. Ginther (135) determined that a bright variation of a Li glass scintillator was a mixture of 26% MgO, 13% $LiO_{0.5}$, 10% $AlO_{1.5}$, 50% SiO_2, and 1% $CeO_{1.5}$, which yielded a light yield of 14% of that of NaI:Tl (nominally 5,000–6,000 photons/MeV). The study by Ginther & Schulman (132) revealed that contaminants in the glass, especially Ca and Ba contaminants, can adversely affect brightness.

Glass scintillators can be machined or formed into various shapes not commonly achieved with crystalline solids. Furthermore, glass scintillators are relatively robust and shock resistant and have relatively constant light yield over a wide range of temperatures. Glass scintillators are used for a variety of applications, including neutron detection, oil well logging, and charged-particle detection in extreme environments. Modern commercial Ce-activated Li glass scintillators can be acquired with different Li activator concentrations and enrichments such as natural Li, 96%-enriched ^{6}Li, and fully depleted ^{6}Li. Glass scintillators with ^{6}Li can be used for combined neutron and gamma-ray detection, whereas glass scintillators depleted of ^{6}Li can be used in mixed radiation fields when neutron-induced counts are undesirable. The decay times generally range between 20 and 105 ns and depend on the Li concentration and the type of radiation particles interacting in the scintillator. These scintillators have higher light yields from electrons than from alpha particles, with an α/β ratio of ~0.23. The light yield of these glass scintillators is reported to be between 8.7% and 13% of that of NaI:Tl.

Boron-based scintillating glasses have been investigated but show lower light yields than do Li glasses (136). Glasses with Tb activators have higher light yields than do Ce-activated glasses, up to 50,000 photons/MeV (35), and are reportedly 2–3 times more radiation hard than Ce-activated glasses. However, the former have long wavelength emissions and long decay times. Eu doping slightly improves light yield relative to Ce doping (137), approximately 110% of that of common GS20 Li glass scintillators. The most probable wavelength of emission is near 450 nm, with a relatively long decay time of 1,230 ns (137).

5. SUMMARY

Scintillators were first used, accidentally, in the discovery of X-rays in 1895. After the discovery of natural radiation the following year, radiation detection methods that used scintillators, including devices such as the spinthariscope, were developed. But most of these detection methods were relatively inconvenient. The commercial introduction of the PMT in 1941, followed by the discovery of NaI:Tl in 1948, changed scintillators into practical radiation spectrometers. After the discovery of NaI:Tl, there was tremendous research activity aimed at discovering additional bright radiation scintillators, and hundreds of scintillators have been documented (see Reference 41 for an example). Yet NaI:Tl remained the best scintillation spectrometer for many decades. However, new and exciting scintillators with properties that in many ways outperform the traditional

Annu. Rev. Mater. Res. 2018.48:245-277. Downloaded from www.annualreviews.org
Access provided by Kansas State University on 09/24/18. For personal use only.

standard NaI:Tl have been discovered and developed relatively recently, proving that this research field is far from closed or saturated. With the introduction of the lanthanide halide, elpasolite, and new ceramic scintillators within the last 20 years, the selection of high-performance scintillation spectrometers has been broadened significantly. Furthermore, there are several commercially available scintillators that are used for special applications such as fast timing, medical imaging, and neutron detection and for measurements in harsh environments. Consequently, scintillation detectors and spectrometers remain an important tool for radiation detection and measurement. Given the recent advancements realized with many new and promising scintillators, the potential for continued discovery and improvement of scintillation materials seems justifiably bright.

DISCLOSURE STATEMENT

The author is not aware of any affiliations, memberships, funding, or financial holdings that might be perceived as affecting the objectivity of this review.

LITERATURE CITED

1. Curran SC, Baker WR. 1944. *A photoelectric alpha particle detector*. Rep. MDDC 1296, US At. Energy Comm.
2. Rodnyi PA. 1997. *Physical Processes in Inorganic Scintillators*. Boca Raton, FL: CRC Press
3. Ridley BK. 1982. *Quantum Processes in Semiconductors*. Oxford, UK: Clarendon Press
4. Lindow JT, Srader E, Farukhi MR. 1978. *Harshaw Scintillation Phosphors*. Solon, OH: Harshaw Chem. Co. 3rd ed.
5. Valais I, Sratos D, Michail C, Konstantinidis A, Kandarakis I, Panayiotakis GS. 2007. Investigation of luminescent properties of LSO:Ce, LYSO:Ce and GSO:Ce crystal scintillators under low-energy gamma-ray excitation used in nuclear imaging. *Nucl. Instrum. Meth. A* 581:99–102
6. Saint-Gobain Cryst. 2016. **https://www.crystals.saint-gobain.com/products/crystal-scintillation-materials**. Accessed Jan. 14
7. Engstrom RW, unknown others. 1980. *Photomultiplier Handbook*. Lancaster, PA: Burle Technol.
8. Renker D. 2006. Geiger-mode avalanche photodiodes, history, properties and problems. *Nucl. Instrum. Meth. A* 567:48–56
9. Birks JB. 1964. *The Theory and Practice of Scintillation Counting*. New York: MacMillan
10. Dorenbos P, De Haas JTM, Van Eijk CWE. 1995. Non-proportionality in the scintillation response and the energy resolution obtainable with scintillation crystals. *IEEE Trans. Nucl. Sci.* 42:2190–202
11. Dorenbos P. 2002. Light output and energy resolution of Ce^{3+}-doped scintillators. *Nucl. Instrum. Meth. A* 486:208–13
12. Kapusta M, Balcerzik M, Moszynski M, Pawelke J. 1999. A high-energy resolution observed from a YAP:Ce scintillator. *Nucl. Instrum. Meth. A* 421:610–13
13. Moszyński M, Kapusta M, Mayhugh M, Wolski D, Flyckt SO. 1997. Absolute light output of scintillators. *IEEE Trans. Nucl. Sci.* 44:1052–61
14. Holl I, Lorenz E, Mageras G. 1988. A measurement of the light yield of common inorganic scintillators. *IEEE Trans. Nucl. Sci.* 35:105–9
15. Mengesha W, Taulbee TD, Rooney BD, Valentine JD. 1998. Light yield nonproportionality of CsI:Tl, CsI(Na) and YAP. *IEEE Trans. Nucl. Sci.* 45:456–61
16. Świderski Ł, Moszyński M, Nassalski A, Syntfeld-Kažuch A, Szczesniak T, et al. 2009. Light yield nonproportionality and energy resolution of praseodymium doped LuAG scintillator. *IEEE Trans. Nucl. Sci.* 56:934–38
17. Payne SA, Moses WW, Sheets S, Ahle L, Cherepy NJ, et al. 2011. Nonproportionality of scintillator detectors: theory and experiment. II. *IEEE Trans. Nucl. Sci.* 58:3392–402
18. Jaffe JE, Jordan DV, Peurrung AJ. 2007. Energy nonlinearity in radiation detection materials: causes and consequences. *Nucl. Instrum. Meth. A* 570:72–83

Annu. Rev. Mater. Res. 2018.48:245-277. Downloaded from www.annualreviews.org
Access provided by Kansas State University on 09/24/18. For personal use only.

Annu. Rev. Mater. Res. 2018.48:245-277. Downloaded from www.annualreviews.org
Access provided by Kansas State University on 09/24/18. For personal use only.

19. Payne SA, Cherepy NJ, Hull G, Valentine JD, Moses WW, et al. 2009. Nonproportionality of scintillator detectors: theory and experiment. *IEEE Trans. Nucl. Sci.* 56:2506–12
20. Moses WW, Bizarri GA, Williams RT, Payne SA, Vasil'ev AN, et al. 2012. The origins of scintillator non-proportionality. *IEEE Trans. Nucl. Sci.* 59:2038–44
21. De Haas JTM, Dorenbos P, Van Eijk CWE. 2005. Measuring the absolute light yield of scintillators. *Nucl. Instrum. Meth. A* 537:97–100
22. Syntfeld A, Moszynski M, Arlt R, Balcerzyk M, Kupusta M, et al. 2005. ^{6}Lil(Eu) in neutron and gamma-ray spectrometry—a highly sensitive thermal neutron detector. *IEEE Trans. Nucl. Sci.* 52:3151–56
23. Hofstadter R, Odell EW, Schmidt CT. 1964. CaI_2 and CaI_2(Eu) scintillation crystals. *Rev. Sci. Instrum.* 35:246–47
24. Hofstadter R, Odell EW, Schmidt CT. 1964. CaI_2 and CaI_2(Eu) scintillation crystals. *IEEE Trans. Nucl. Sci.* 11:12–14
25. Zdesenko YG, Avignone FT, Brudanin VB, Danevich FA, Nagorny SS, et al. 2005. Scintillation properties and radioactive contamination of $CaWO_4$ crystal scintillators. *Nucl. Instrum. Meth. A* 538:657–67
26. Cherepy NJ, Payne SA, Asztalos SJ, Hull G, Kuntz JD, et al. 2009. Scintillators with potential to supersede lanthanum bromide. *IEEE Trans. Nucl. Sci.* 56:873–80
27. Baryshevsky VG, Korzhik MV, Moroz VI, Pavlenko VB, Fyodorov AA, et al. 1991. $YAlO_3$:Ce-fast-acting scintillators for detection of ionizing radiation. *Nucl. Instrum. Meth. B* 58:291–93
28. Leroq P, Annenkov A, Gektin A, Korzhik M, Pedrini C. 2006. *Inorganic Scintillators for Detector Systems*. Berlin: Springer
29. Shah KS, Glodo J, Higgins W, Van Loef EVD, Moses W, et al. 2005. $CeBr_3$ scintillators for gamma-ray spectroscopy. *IEEE Trans. Nucl. Sci.* 52:3157–59
30. Moszyński M, Wolski D, Ludziejewski T, Kapusta M, Lempicki A, et al. 1997. Properties of the new LuAP:Ce scintillator. *Nucl. Instrum. Meth. A* 385:123–31
31. Drozdowski W, Dorenbos P, De Haas JTM. 2008. Scintillation properties of praseodymium activated $Lu_3Al_5O_{12}$ single crystals. *IEEE Trans. Nucl. Sci.* 55:2420–24
32. Nikl M, Yoshokawa A, Kamada K, Nejezchleb K, Stanek CR, et al. 2013. Development of LuAG-based scintillator crystals—a review. *Prog. Cryst. Growth Charact. Mater.* 59:47–72
33. Combes CM, Dorenbos P, Van Eijk CWE, Krämer KW, Güdel HU. 1999. Optical and scintillation properties of pure and of Ce^{3+}-doped Cs_2LiYCl_6 and Li_3YCl_6:Ce^{3+} crystals. *J. Lumin.* 82:299–305
34. Scintacor. 2016. *6-lithium glass*. **https://scintacor.com/products/6-lithium-glass/**
35. Pavan P, Zanella G, Zannoni R, Polato P. 1991. Radiation damage and annealing of scintillating glasses. *Nucl. Instrum. Meth. B* 61:487–90
36. Li Q, Grim JQ, Williams RT, Bizarri GA, Moses WW. 2011. A transport-based model of material trends in nonproportionality of scintillators. *J. Appl. Phys.* 109:123716
37. Valentine JD, Rooney BD, Li J. 1998. The light yield nonproportionality component of scintillator energy resolution. *IEEE Trans. Nucl. Sci.* 45:512–17
38. Melcher CL. 1989. Scintillators for well logging applications. *Nucl. Instrum. Meth. B* 40–41:1214–18
39. NIST XCOM. 2016. *Element/compound/mixture selection*. **https://physics.nist.gov/PhysRefData/Xcom/html/xcom1.html**. Accessed June 1
40. Derenzo S, Moses WW, Cahoon JL, DeVol TA, Boatner L. 1991. *X-ray fluorescence measurements of 412 inorganic compounds*. IEEE Nucl. Sci. Symp. Conf. Rec., 1:143–47
41. Derenzo S, Boswell M, Weber M, Brennan K. 2016. *Scintillation properties*. **http://scintillator.lbl.gov**. Accessed Feb. 25
42. Hofstadter R. 1948. Alkali halide scintillation counters. *Phys. Rev.* 74:100–1
43. Koički S, Koički A, Ajdačić A. 1973. The investigation of the 0.15s phosphorescence component of NaI:Tl and its application in scintillation counting. *Nucl. Instrum. Meth.* 108:297–99
44. Van Sciver WJ. 1956. Alkali halide scintillators. *IRE Trans. Nucl. Sci.* 3:39–50
45. Van Sciver WJ, Bogart L. 1958. Fundamental studies of scintillation phenomenon in NaI. *IRE Trans. Nucl. Sci.* 5:90–92
46. Moszyński M, Balcerzyk M, Czarnacki W, Kapusta M, Klamra W, et al. 2003. Study of pure NaI at room and liquid nitrogen temperatures. *IEEE Trans. Nucl. Sci.* 50:767–73

Annu. Rev. Mater. Res. 2018.48:245-277. Downloaded from www.annualreviews.org
Access provided by Kansas State University on 09/24/18. For personal use only.

47. Moszyński M, Czarnacki W, Klamra W, Szawlowski M, Schotanus P, Kapusta M. 2003. Intrinsic energy resolution of pure NaI studied with large area avalanche photodiodes at liquid nitrogen temperatures. *Nucl. Instrum. Meth. A* 505:63–67
48. Moszyński M, Czarnacki M, Kapusta M, Szawlowski M, Klamra W, Schotanus P. 2002. Energy resolution and light yield non-proportionality of pure NaI scintillator studied with large area avalanche photodiodes at liquid nitrogen temperatures. *Nucl. Instrum. Meth. A* 486:13–17
49. Bonanomi J, Rossel J. 1952. Scintillations de luminescence dans les iodures d'alcalins. *Helv. Phys. Acta* 25:725–52
50. Jing T, Cho G, Drewery J, Fujieda I, Kaplan SN, et al. 1992. Enhanced columnar structure in CsI layer by substrate patterning. *IEEE Trans. Nucl. Sci.* 39:1195–98
51. Nagarkar VV, Gupta TK, Miller SR, Klugerman Y, Squillante MR, Entine G. 1998. Structured CsI:Tl scintillators for X-ray imaging applications. *IEEE Trans. Nucl. Sci.* 45:492–96
52. Amsler C, Grögler D, Joffrain W, Lindelöf D, Marchesotti M, et al. 2002. Temperature dependence of pure Cs:I scintillation light yield and decay time. *Nucl. Instrum. Meth. A* 480:494–500
53. Khan S, Kim HJ, Kim YD. 2015. Scintillation characterization of thallium-doped lithium iodide crystals. *Nucl. Instrum. Meth. A* 793:31–34
54. Robertson JC, Lynch JG, Jack W. 1961. The luminescence of CsBr(Tl) and CsI:Tl as a function of temperature. *Proc. Phys. Soc.* 78:1188–94
55. Cook JR, Mahmoud KA. 1954. Luminescence characteristics of some scintillating crystals. *Proc. Phys. Soc.* 67:817–24
56. Van Sciver WJ, Hofstadter R. 1952. Gamma- and alpha-produced scintillations in cesium fluoride. *Phys. Rev.* 87:522
57. Moszyński M, Allemand R, Odru MLR, Vacher J. 1983. Recent progress in fast timing with CsF scintillators in application to time-of-flight positron tomography in medicine. *Nucl. Instrum. Meth.* 205:239–49
58. Van Eijk CWE, Andriessen J, Dorenbos P, Jansons J, Khaidukov NM, et al. 1993. Experimental and theoretical studies of cross luminescence. In *Heavy Scintillators for Scientific and Industrial Applications: Proceedings of the "Cristal 2000" International Workshop*, ed. F De Notaristefani, P Lecoq, M Schneegans, pp. 161–66. Gif-sur-Yvette, Fr.: Ed. Front.
59. Milton JCD, Hofstadter R. 1949. Luminescent spectra of phosphors useful in scintillation counters. *Phys. Rev.* 75:1289–90
60. Smolśkaya LP, Shuraleva EI, Parfianovich IA. 1969. Radiation of paired centers in the phosphor KI(Tl). *Sov. Phys. J.* 12:1063–65
61. Robertson JC, Lynch JG. 1961. The luminescent decay of various crystals for particles of different ionization density. *Proc. Phys. Soc.* 77:751–56
62. Ishii M, Kobayashi M. 1991. Single crystals for radiation detectors. *Prog. Cryst. Growth Charact. Mater.* 23:245–311
63. Messner D, Smakula A. 1960. Color center in alkaline earth fluorides. *Phys. Rev.* 120:1162–66
64. Heath DF, Sacher PA. 1966. Effects of a simulated high-energy space environment on the ultraviolet transmittance of optical materials between 1050 Å and 3000 Å. *Appl. Opt.* 5:937–43
65. Majewski S, Anderson D. 1985. Radiation damage test of barium fluoride scintillator. *Nucl. Instrum. Meth. A* 241:76–79
66. Woody CL, Levy PW, Klerstead JA. 1989. Slow component suppression and radiation damage in doped BaF_2 crystals. *IEEE Trans. Nucl. Sci.* 36:536–42
67. Murashita M, Saitoh H, Tobimatsu K, Chiba M, Hirose T, et al. 1986. Performance and radiation damage of a BaF_2 calorimeter. *Nucl. Instrum. Meth. A* 243:67–76
68. Schotanus P, Van Eijk CWE, Hollander RW, Pijpelink J. 1985. Temperature dependence of BaF_2 scintillation light yield. *Nucl. Instrum. Meth. A* 238:564–65
69. Colmenares C, Shapiro EG, Barry PE, Prevo CT. 1974. A europium-doped, calcium-fluoride scintillator system for low-level tritium detection. *Nucl. Instrum. Meth.* 114:277–89
70. Van Sciver WJ, Hofstadter R. 1951. Scintillations in thallium-activated CaI_2 and CsI*. *Phys. Rev.* 84:1062–63
71. Hofstadter R. 1967. *Europium activated calcium iodide scintillators*. US Patent 3,342,745

Annu. Rev. Mater. Res. 2018.48:245-277. Downloaded from www.annualreviews.org
Access provided by Kansas State University on 09/24/18. For personal use only.

72. Boatner LA, Ramey JO, Kolopus JA, Neal JS. 2015. Divalent europium doped and un-doped calcium iodide scintillators: scintillator characterization and single crystal growth. *Nucl. Instrum. Meth. A* 786:23–31
73. Hofstadter R. 1968. *Europium activated strontium iodide scintillators*. US Patent 3,373,270
74. Alekhin MS, De Haas JTM, Krämer KW, Dorenbos P. 2011. Scintillation properties of and self absorption in SrI_2:Eu^{2+}. *IEEE Trans. Nucl. Sci.* 58:2519–27
75. Kawai T, Sakuragi S, Hashimoto S. 2016. Luminescence properties of pure and Eu-doped SrI_2 crystals purified by a "liquinert" process and grown by vertical Bridgman method. *J. Lumin.* 176:58–64
76. Muthman W, Stützel L. 1899. Eine Enfache Methode zer Darstellung der Schwefel-, Chlor- und Brom-Verbindungen der Ceritmetalle. *Ber. Dtsch. Chem. Ges.* 32:3413–19
77. Doty FP, McGregor DS, Harrison M, Findley K, Polichar R. 2007. Structure and properties of lanthanide halides. *Proc. SPIE* 6707:670–705
78. Harrison MJ, Linnick C, Montag B, Brinton S, McCreary M, et al. 2009. Scintillation performance of aliovalently doped $CeBr_3$. *IEEE Trans. Nucl. Sci.* 56:1661–65
79. Guss P, Foster ME, Wong BM, Doty FP, Shah K, et al. 2014. Results for aliovalent doping of $CeBr_3$ with Ca^{2+}. *J. Appl. Phys.* 115:034908
80. Van Loef EVD, Dorenbos P, Van Eijk CWE, Krämer K, Gübel HU. 2001. Scintillation properties of $LaCl_3$:Ce^{3+} crystals: fast, efficient, and high-resolution scintillators. *IEEE Trans. Nucl. Sci.* 48:342–45
81. Van Loef EVD, Dorenbos P, Van Eijk CWE, Krämer K, Gübel HU. 2002. Scintillation properties of $LaBr_3$:Ce^{3+} crystals: fast, efficient, and high-energy-resolution scintillators. *Nucl. Instrum. Meth. A* 486:254–58
82. Balcerzyk M, Moszyński M, Galazka Z, Kapusta M, Syntfeld A, Lefaucheur J-L. 2005. Perspectives for high resolution and high light output LuAP:Ce crystals. *IEEE Trans. Nucl. Sci.* 52:1823–29
83. Autrata R, Schauer P, Kvapil J, Kvapil J. 1978. A single crystal of YAG—new fast scintillator in SEM. *J. Phys. E Sci. Instrum.* 11:707–8
84. Bok J, Schauer P. 2014. Performance of SEM scintillation detector evaluated by modulation transfer function and detective quantum efficiency function. *Scanning* 36:384–93
85. Ludziejewski T, Moszyński M, Wolski D, Klamra W, Moszyńska K. 1997. Investigation of some scintillation properties of YAP:Ce crystals. *Nucl. Instrum. Meth. A* 345:287–94
86. Moszyński M, Ludziejewski T, Wolski D, Klamra W, Norlin LO. 1994. Properties of the YAP:Ce scintillator. *Nucl. Instrum. Meth. A* 345:461–67
87. Chewpraditkul W, Swiderski L, Moszyński M, Szczesniak T, Syntfeld-Kazuch A, et al. 2009. Scintillation properties of LuAG:Ce, YAG:Ce and LYSO:Ce crystals for gamma-ray detection. *IEEE Trans. Nucl. Sci.* 56:3800–5
88. Yanagida T, Fukabori A, Fujimoto Y, Ikesue A, Kamada K, et al. 2011. Scintillation properties of transparent $Lu_3Al_5O_{12}$ ceramics doped with different concentrations of Pr^{3+}. *Phys. Status Solid. C* 8:140–43
89. Furukawa Denshi Co. 2016. *Pr:LuAG scintillator crystal*. Note, Furukawa Denshi. **http://www.furukawa-denshi.co.jp/cgi-bin/pdfdata/20140428162950.pdf**
90. Cho ZH, Farukhi MR. 1977. Bismuth germanate as a potential scintillation detector in positron cameras. *J. Nucl. Med.* 18:840–44
91. Nestor OH, Huang CY. 1975. Bismuth germanate: a high-Z gamma-ray and charged particle detector. *IEEE Trans. Nucl. Sci.* 22:68–71
92. Weber MJ, Monchamp RR. 1973. Luminescence of $Bi_4Ge_3O_{12}$: spectral and decay properties. *J. Appl. Phys.* 44:5495–99
93. Melcher CL, Schweitzer JS, Peterson CA, Manente RA, Suzuki H. 1996. Crystal growth and scintillation properties of the rare earth oxyorthosilicates. In *Proceedings of the International Conference on Inorganic Scintillators and Their Applications* (SCINT95), ed. P Dorenbos, CWE van Eijk, pp. 309–15. Delft, Neth.: Delft Univ. Press
94. Kamae T, Fukazawa Y, Isobe N, Kokubun M, Kubota A, et al. 2002. Improvement on the light yield of a high-Z inorganic scintillator GSO(Ce). *Nucl. Instrum. Meth. A* 490:456–64
95. Shimura N, Kamada M, Gunji A, Yamana S, Usui T, et al. 2006. Zr doped GSO:Ce single crystals and their scintillation performance. *IEEE Trans. Nucl. Sci.* 53:2519–22

Annu. Rev. Mater. Res. 2018.48:245-277. Downloaded from www.annualreviews.org
Access provided by Kansas State University on 09/24/18. For personal use only.

96. Roscoe B, Grau JA, Manente RA, Melcher CL, Peterson CA, et al. 1992. Use of GSO for inelastic gamma-ray spectroscopy measurements in the borehole. *IEEE Trans. Nucl. Sci.* 39:1412–16
97. Ficke DC, Ter-Pogossian MM, Miyaoka RS, Lewellen TK. 1994. A GSO(Ce) block type detector for high count rate PET applications. *IEEE Trans. Nucl. Sci.* 4:1859–63
98. Balcerzyk M, Moszyński M, Kapusta M, Wolski D, Pawelke J, Melcher CL. 2000. YSO, LSO, GSO and LGSO. A study of energy resolution and nonproportionality. *IEEE Trans. Nucl. Sci.* 47:1319–23
99. Reeder PL. 1994. Thin GSO scintillator for neutron detection. *Nucl. Instrum. Meth.* 353:134–36
100. Melcher CL. 1990. *Lutetium orthosilicate single crystal scintillator detector*. US Patent 4,958,080
101. Melcher CL. 1991. *Lutetium orthosilicate single crystal scintillator detector*. US Patent 5,025,151
102. Melcher CL, Schweitzer JS. 1992. Cerium-doped lutetium oxyorthosilicate: a fast, efficient new scintillator. *IEEE Trans. Nucl. Sci.* 39:502–5
103. Daghighian F, Shenderov P, Pentlow KS, Graham MC, Eshaghian B, et al. 1993. Evaluation of cerium doped lutetium oxyorthosilicate (LSO) scintillation crystal for PET. *IEEE Trans. Nucl. Sci.* 40:1045–47
104. Szupeyczynski P, Melcher CL, Spurrier MA, Maskarinec MP, Carey AA, et al. 2004. Thermoluminescence and scintillation properties of rare earth oxyorthosilicate scintillators. *IEEE Trans. Nucl. Sci.* 51:1103–10
105. Nassalski A, Kapusta M, Batsch T, Wolski D, Möckel D, et al. 2007. Comparative study of scintillators for PET/CT detectors. *IEEE Trans. Nucl. Sci.* 54:3–10
106. Cutler PA, Melcher CL, Spurrier MA, Szupryczynski P, Eriksson LA. 2009. Scintillation nonproportionality of lutetium- and yttrium-based silicates and aluminates. *IEEE Trans. Nucl. Sci.* 56:915–19
107. Dahlbom M, MacDonald LR, Eriksson L, Paulus M, Andreaco M, et al. 1997. Performance of a YSO/LSO phoswich detector for use in a PET/SPECT system. *IEEE Trans. Nucl. Sci.* 44:1114–19
108. Cooke DW, McClellan KJ, Bennett Bl, Roper JM, Whittaker MT, et al. 2000. Crystal growth and optical characterization of cerium-doped $Lu_{1.8}Y_0.2SiO_5$. *J. Appl. Phys.* 88:7360–62
109. Pepin CM, Bérad P, Perrot A-L, Pépin C, Houde D, et al. 2004. Properties of LYSO and recent LSO scintillators for phoswich PET detectors. *IEEE Trans. Nucl. Sci.* 51:789–95
110. Chen J, Zhang L, Zhu R. 2007. Large size LSO and LYSO crystal scintillators for future high-energy physics and nuclear physics experiments. *Nucl. Instrum. Meth. A* 572:218–24
111. Rexon Compon. 2015. *LYSO/LSO technical specifications*. **http://www.rexon.com/LSOBLANKSPEC.pdf**. Accessed Sept. 28
112. Omega Piezo. 2018. *BGO and LYSO crystals*. **http://www.omegapiezo.com/crystal-scintillators/**. Accessed May 2
113. RMD. 2016. *Gamma-neutron scintillation detector*. **http://rmdinc.com/wp-content/uploads/2014/10/CLYC-Properties-PDF.pdf**. Accessed Feb. 25
114. Bessiere A, Dorenbos P, Van Eijk CWE, Krämer KW, Güdel HU. 2005. Luminescence and scintillation properties of $Cs_2LiYCl_6:Ce^{3+}$ for gamma and neutron detection. *Nucl. Instrum. Meth. A* 537:242–46
115. Shirwadkar U, Glodo J, Van Loef EVD, Hawrami R, Mukhopadhyay S, et al. 2011. Scintillation properties of $Cs_2LiLaBr_6$ (CLLB) crystals with varying Ce^{3+} concentration. *Nucl. Instrum. Meth. A* 652:268–70
116. Shirwadkar U, Hawrami R, Glodo J, Van Loef EVD, Shah KS. 2012. Novel scintillation material $Cs_2LiLaBr_{6-x}Cl_x$:Ce for gamma-ray and neutron spectroscopy. In *IEEE Nucl. Sci. Symp. Med. Imag. Conf. Rec.*, Anaheim, CA, Oct. 21–Nov. 3, Pap. N41-1
117. Glodo J, Van Loef E, Hawrami R, Higgins WM, Churilov A, et al. 2011. Selected properties of Cs_2LiYCl_6, $Cs_2LiLaCl_6$, and $Cs_2LiLaBr_6$ scintillators. *IEEE Trans. Nucl. Sci.* 58:333–38
118. Doty FP, Zhou X, Yang P, Rodriguez MA. 2012. *Elpasolite scintillators*. Rep. SAND2012-9951, Sandia Natl. Lab.
119. Kerisit SN, Gao F, Xie YL, Campbell LW, Wu D, Prange MP. 2014. *Science-driven candidate search for new scintillator materials: FY 2014 annual report*. Rep. PNNL-23752, Pac. Northwest Natl. Lab.
120. Gundiah G, Brennan K, Yan Z, Samulon EC, Wu G, et al. 2014. Structure and scintillation properties of Ce^{3+}-activated $Cs_2NaLaCl_6$, Cs_3LaCl_6, $Cs_2NaLaBr_6$, Cs_3LaBr_6, Cs_2NaLaI_6, and Cs_3LaI_6. *J. Lumin.* 149:374–84
121. Birowosuto MD, Dorenbos P, De Haas JTM, Van Eijk CWE, Krämer KW, Güdel HU. 2008. Li-based thermal neutron scintillator research: $Rb_2LiYBr_6:Ce^{3+}$ and other elpasolites. *IEEE Trans. Nucl. Sci.* 55:1152–55

122. Van Eijk CWE, De Haas JTM, Dorenbos P, Krämer KW, Güdel HU. 2005. Development of elpasolite and monoclinic thermal neutron scintillators. In *IEEE Nucl. Sci. Symp. Conf. Rec.*, Puerto Rico, Oct. 23–29, pp. 239–43
123. Cusano DA, Holub FF, Prochazka S. 1980. *Ceramic-like scintillators*. US Patent 4,242,221
124. DiBianca FA, Georges J-PJ, Cusano DA, Greskovich CD. 1985. *Rare earth ceramic scintillator*. US Patent 4,525,626
125. Greskovich C, Duclos S. 1997. Ceramic scintillators. *Annu. Rev. Mater. Sci.* 27:69–88
126. Lempicki A, Brecher C, Szupryczynski P, Lingertat H, Nagarkar VV, et al. 2002. A new lutetia-based ceramic scintillator for X-ray imaging. *Nucl. Instrum. Meth. A* 488:579–90
127. Duclos SJ, Greskovich CD, Lyons RJ, Vartuli JS, Hoffman DM, et al. 2003. Development of the HiLight^{TM} scintillator for computed tomography medical imaging. *Nucl. Instrum. Meth. A* 505:68–71
128. Cherepy NJ, Kuntz JD, Roberts JJ, Hurst TA, Drury OB, et al. 2008. *Transparent ceramic scintillator fabrication, properties and applications*. Rep. LLNL-PROC-406543, Lawrence Livermore Natl. Lab.
129. Cherepy NJ, Seeley ZM, Payne SA, Beck PR, Swanberg EL, et al. 2014. *High energy resolution transparent ceramic garnet scintillators*. Rep. LLNL-PROC-659775, Lawrence Livermore Natl. Lab.
130. Cherepy NJ. 2015. *Transparent ceramic scintillators for gamma spectroscopy and MeV imaging*. Rep. LLNL-PROC-676780, Lawrence Livermore Natl. Lab.
131. Cherepy NJ, Payne SA, Sturm BW, O'Neal SP, Seeley ZM, et al. 2011. Performance of europium-doped strontium iodide, transparent ceramics and bismuth-loaded polymer scintillators. *Proc. SPIE* 8142:81420W
132. Ginther RJ, Schulman JH. 1958. Glass scintillators. *IRE Trans. Nucl. Sci.* 5:92–95
133. Voitovetskii VK, Tolmacheva NS, Arsaev MI. 1960. Scintillating glass for the detection of slow neutrons. *Sov. J. At. Energy* 6:203–7
134. Voitovetskii VK, Tolmacheva NS. 1960. Lithium silicate scintillating glasses for the detection of slow neutrons. *Soviet J. At. Energy* 6:335–36
135. Ginther RJ. 1960. New cerium activated scintillating glasses. *IRE Trans. Nucl. Sci.* 7:28–31
136. Bollinger LM, Thomas GE, Ginther RJ. 1962. Neutron detection with glass scintillators. *Nucl. Instrum. Meth.* 17:97–116
137. Fujimoto Y, Yanagida T, Koshimizu M, Asai K. 2015. Photoluminescence and scintillation properties of SiO_2 glass activated with Eu^{2+}. *Sens. Mater.* 27:263–68
138. Syntfeld-Każuch A, Sibczyński P, Moszyński M, Gektin AV, Czarnacki W, et al. 2010. Energy resolution of CsI(Na) scintillators. *Rad. Meas.* 45:377–79

Annu. Rev. Mater. Res. 2018.48:245-277. Downloaded from www.annualreviews.org
Access provided by Kansas State University on 09/24/18. For personal use only.

Annual Review of Materials Research

Volume 48, 2018

Contents

First-Principles Calculations of Point Defects for Quantum Technologies
Cyrus E. Dreyer, Audrius Alkauskas, John L. Lyons, Anderson Janotti, and Chris G. Van de Walle 1

First-Principles Statistical Mechanics of Multicomponent Crystals
A. Van der Ven, J.C. Thomas, B. Puchala, and A.R. Natarajan 27

Design Considerations for Artificial Water Channel–Based Membranes
Woochul Song, Chao Lang, Yue-xiao Shen, and Manish Kumar 57

Recent Advances in Zeolitic Membranes
Robert Bedard and Chunqing Liu 83

The Diversity of Layered Halide Perovskites
Matthew D. Smith, Ethan J. Crace, Adam Jaffe, and Hemamala I. Karunadasa 111

Electrochemical and Chemical Insertion for Energy Transformation and Switching
Yiyang Li and William C. Chueh 137

Hard X-Ray Photon Correlation Spectroscopy Methods for Materials Studies
Alec R. Sandy, Qingteng Zhang, and Laurence B. Lurio 167

High-Performance Piezoelectric Crystals, Ceramics, and Films
Susan Trolier-McKinstry, Shujun Zhang, Andrew J. Bell, and Xiaoli Tan 191

High-Temperature Dielectric Materials for Electrical Energy Storage
Qi Li, Fang-Zhou Yao, Yang Liu, Guangzu Zhang, Hong Wang, and Qing Wang ... 219

Materials for Gamma-Ray Spectrometers: Inorganic Scintillators
Douglas S. McGregor 245

Optical Metasurfaces: Progress and Applications
Shengyuan Chang, Xuexue Guo, and Xingjie Ni 279

Property Engineering in Perovskites via Modification of Anion Chemistry
Yoji Kobayashi, Yoshihiro Tsujimoto, and Hiroshi Kageyama 303

Annu. Rev. Mater. Res. 2018.48:245-277. Downloaded from www.annualreviews.org
Access provided by Kansas State University on 09/24/18. For personal use only.

Simulation of Crystallization of Biominerals
Raffaella Demichelis, Alicia Schuitemaker, Natalya A. Garcia, Katarzyna B. Koziara, Marco De La Pierre, Paolo Raiteri, and Julian D. Gale 327

Indexes

Cumulative Index of Contributing Authors, Volumes 44–48 353

Errata

An online log of corrections to *Annual Review of Materials Research* articles may be found at http://www.annualreviews.org/errata/matsci

Annu. Rev. Mater. Res. 2018.48:245-277. Downloaded from www.annualreviews.org
Access provided by Kansas State University on 09/24/18. For personal use only.